$B^o - \bar{B}^o$ Mixing at the Z^o pole

Simon John Patton

Imperial College, London

A thesis submitted for the degree of

Doctor of Philosophy

at the University of London

September 1991

$B^o - \bar{B}^o$ Mixing at the Z^o pole

Simon John Patton

Imperial College, London

Abstract

This thesis presents a new method of investigating the phenomena of $B^0 - \bar{B}^0$ mixing at e^+e^- colliders operating at centre-of-mass energies significantly above the $\Upsilon(4S)$ mass. It also investigates the z readout of ALEPH's Inner Tracking Chamber.

The z readout of the ITC is shown to be working well and a non-linearity, known as the S-bend, is measured to have an amplitude of 8.2 cm and a period of 173 cm.

The new method of examining $B^0 - \bar{B}^0$ mixing determines the type of b quark in a decaying hadron by its semileptonic decay. The type of b quark in the opposite hadron is determined by means of a momentum weighted hemisphere charge. This method is applied to the data taken by ALEPH in 1989 and 1990 to give a 90% confidence limit on the mixing parameter χ of $0.084 \leq \chi \leq 0.175$.

Combining the result of this new method with previously published measurements of $B^0 - \bar{B}^0$ mixing leads to $\chi_d = 0.18 \pm 0.05$ and $\chi_s = 0.45 \pm 0.24$ if it is assumed that $f_d = 0.375$ and $f_s = 0.150$ at LEP energies. Also measured is a lower limit on χ_s of $\chi_s > 0.07$, with a 90% confidence limit.

To my father.

At the age of 7, when I discovered $\sqrt{-1}$ on his calculator gave an error, he explained complex numbers to me. I didn't understand them then either.

Acknowledgements

This thesis would not have been possible without the help of a variety of people, many of whom are mentioned below. (To those that I have missed out "Oops" and more probably "I owe you a pint".)

The first to thank is Prof. Dave Binnie who let me loose on an unsuspecting physics world by letting me join the Group. The members of which have helped me in so many different ways. In particular I would like to thank my supervisor John for his encouragement, comments and signature. Also Bill C. and Julia for their time while I was working on the ITC. Thanks also goes to the Great British Taxpayer who funded me throughout this time via the offices of the S.E.R.C.

My thanks goes to Bill A. for his initial idea for this analysis, and to Witold and Toby for all their work and thoughts on it throughout. Special thanks is given to Ingrid who read through most of this and gave me many useful comments, despite having other pressing issues on hand at the time.

On the organisational side of things I'd like to thank Linda and Diane for getting me to and from CERN whenever it was required. Without Sue and Mary Elizabeth life in Genève would have been infinitely more confusing and impossible.

To those who dragged me out of my office at CERN (kicking and screaming!), thanks. That includes Martin ("That rich B&$*!d"), Alan ("we can leave before closing time"), Ingrid ("Marvin"), Roger ("not Rog"), Mim ("Time to let my hair down"), Nigel ("Lets trash this joint"), Tony ("Time for a coffee"), Nat ("As in whisky"), Bish ("Miss moral watchdog") and others.

Away from physics, I'd like to mention Kev ("Mighty Quagloop.C, Lord of Chaos, *et al.*"), Ilya ("R.P. Aldrya"), Cathy ("You old tart"), Cathy ("You should see N.Z."), Clare ("without an 'i' "). I'd also like to thank Beth and Graham for their various lifts to and from everywhere.

A very special thanks goes to Ruth, who would always remind me why I was

doing this and stopped me doing anything too rash.

Finally, and most importantly, I'd like to thank my Mother. She has had to put up with all sorts of stupidity, especially when I decided to do this rather than get a "real" job, but she has yet to disown me (Don't ask me why!). Thanks Mum.

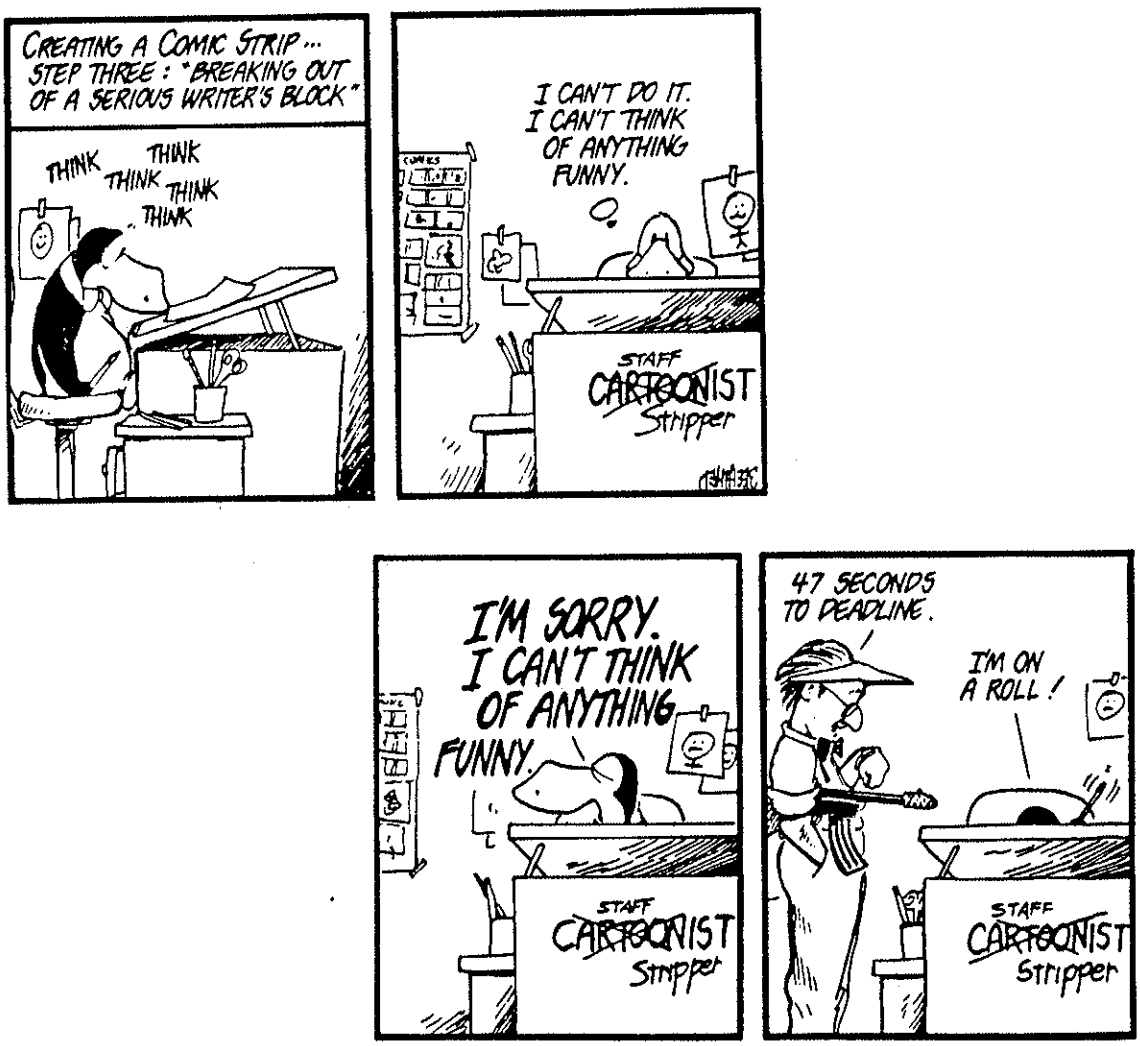

Contents

List of Figures

List of Tables

Chapter 1

Introduction

The phenomenon where a meson is created as a B^0 but decays as a $\bar{B}^0$ and vice versa is known as $B^0 - \bar{B}^0$ mixing. To measure this it is necessary to know the type of quark, either a b quark or its antiparticle a $\bar{b}$ quark, in both the initial and final mesons. The fact that b quarks are created in quark–antiquark pairs can be used to derive information about the initial quark in a B meson; while the decay mode of the final meson can be used to discover the type of quark which it contained. Traditionally leptons from the semileptonic decay of b quarks (see Figure 1.1) have been used to identify the types of decaying quarks on both sides of an event. If both quarks are of the same type then mixing on one side must

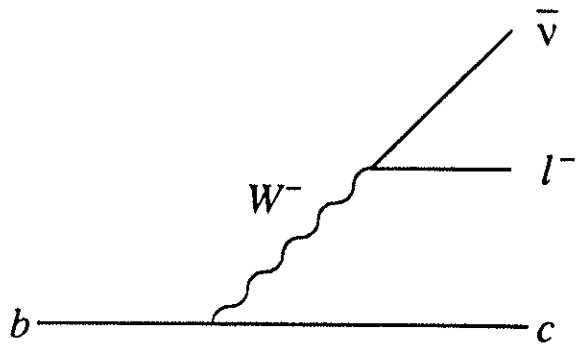

Figure 1.1: *Schematic of the semileptonic decay of a b quark.*

have occurred. This method of investigating $B^0 - \bar{B}^0$ mixing is referred to as the 'dilepton' method.

A B meson decays into an electron or muon 23% of the time[1]. Therefore, assuming all b quarks form B mesons, only 5% of $b\bar{b}$ events can be used in a dilepton analysis. Moreover the experimental efficiency for identifying the leptons from a semileptonic decay of a B is usually about 50% so that only around 1.3% of $b\bar{b}$ events can be used in that type of analysis. A new method of investigating $B^0 - \bar{B}^0$ mixing is presented in this thesis. This new method only requires that one of the B mesons decays semileptonically so that about 12% of the $b\bar{b}$ events can be used.

1.1 Overview of method

The philosophy of this thesis is to describe each of the components of the method separately and then bring them all together. This allows the various different parts to be used in other analyses without having to be first disentangled from any particular one. Moreover it allows the reader to understand each topic as it is discussed without having to worry about how it fits into the rest of the method. However some people find it easier to follow an idea when it is seen within the context of the final result. Therefore an overview of the method is given in this section.

As previously stated the charge of a lepton from a semileptonic decay of a b quark can be used to identify the type of quark in the final B meson. In this method the lepton is used to flag the type of b quark that decayed on one side of an event. The type of quark created on the other side of the event will be of the opposite type to the initial quark in the lepton's B meson. Instead of using another semileptonic decay to identify the type of quark on the opposite side, a momentum weighted hemisphere charge is used. This hemisphere charge reflects, to a certain extent, the sign of the charge of the initial quark in that hemisphere, thus allowing the type of quark to be determined. The charge of

the lepton can be combined with the hemisphere charge of the opposite side of the event in order to give a quantity called the lepton–signed hemisphere charge. If the hemisphere charge perfectly reflected the charge of the initial quark then the number of positive to negative lepton–signed hemisphere charges would give a measurement of the amount of mixing in the sample. However the hemisphere charge only reflects the initial quark's charge in a statistical sense so there will be some dilution in the result of this method. This dilution tends to be offset by the increase in the number of useable events. In Chapter 7 it will be seen that for the data used in this thesis this method has a similar power as the dilepton method.

1.2 Layout of thesis

As well as presenting a new method of investigating $B^0 - \bar{B}^0$ mixing this thesis also applies the method to data taken by the ALEPH detector during 1989 and 1990. Therefore a description of this detector and how the data are handled is given in Chapter 2. Chapter 3 gives a detailed description of the study done by the author on the readout of the z coordinate of the Inner Tracking Chamber of ALEPH in preparation for a 3 dimensional trigger processor.

A summary of the theoretical framework of $B^0 - \bar{B}^0$ mixing within current theories is given in Chapter 4. Also discussed in this chapter are the various parameters that are used to describe $B^0 - \bar{B}^0$ mixing and how they are related.

The components of the method are explained and investigated in Chapters 5 and 6. Chapter 5 deals with the determination of the initial quark charge using a momentum weighted hemisphere charge. Chapter 6 covers the identification of leptons and the tagging of $b\bar{b}$ events. It also draws together all the parts of the method to produce a measurement of $B^0 - \bar{B}^0$ mixing and this is followed by a discussion of the systematic errors of the method.

In Chapter 7, the result for this new method is combined with the results from ALEPH's dileptons analysis and the ARGUS and CLEO measurements for

mixing in the B_d^0 system to give measurements of mixing in both the B_d^0 and B_s^0 systems.

Finally Chapter 8 discusses the conclusion derived from this analysis.

1.3 Charge conjugation

Throughout this thesis whenever a process is discussed its charge conjugate is also implied. However, due to the nature of the topic of this thesis, care must be taken to conjugate the whole process. For instance stating "a B^0 mixes into a $\bar{B}^0$" also implies "a $\bar{B}^0$ mixes into a B^0" but not " a $\bar{B}^0$ mixes into a $\bar{B}^0$". Moreover from Chapter 5 onwards when a sample is referred to as containing B^0's it will also contain the equivalent $\bar{B}^0$'s.

The convention used throughout this thesis is that a B_d^0 meson contains an $\bar{b}$ quark and a d quark. Similarly a B_s^0 meson contains a $\bar{b}$ quark and an s quark.

Chapter 2

ALEPH - Apparatus for LEp PHysics

ALEPH is an international collaboration of thirty physics institutes, studying the physics of e^+e^- interactions on CERN's LEP accelerator.

2.1 LEP - Large Electron Positron collider

LEP (the Large Electron Positron collider) is the latest and largest of CERN's colliding ring accelerators. It is a near circular ring which is almost 27 km in circumference.

LEP was designed to accelerate and collide beams of electrons and positrons with centre-of-mass energies of up to 200 GeV. However, it is initially being operated at centre-of-mass energies around 92 GeV, the mass of the Z^0 boson. Both the electrons and positrons, after injection from a linac, are accelerated by CERN's smaller PS and SPS accelerators. The SPS delivers the leptons in packets to LEP with an energy of 20 GeV. LEP collects these packets into two beams, one containing electrons the other containing the positrons, each made up of four bunches. LEP accumulates leptons until it has a sufficient number of particles, typically around 1.5 mA for each beam, to give a good luminosity. These are then accelerated up to an energy of about 46 GeV to give collisions around 92 GeV. Once the beams are accelerated they are focused (known as squeezing) and collided at chosen interaction points, where physics events can then be recorded.

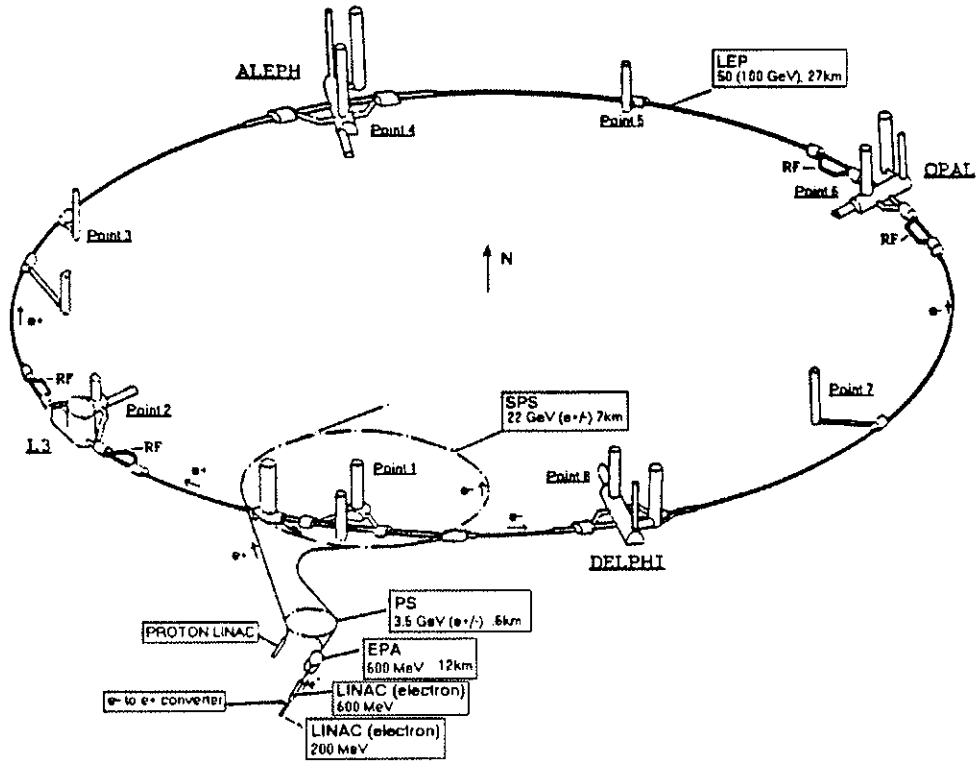

Figure 2.1: *LEP and the other accelerators used to generate beams of 50 GeV leptons.*

There are 8 points around LEP where the beams can intersect. These points are shown in Figure 2.1 along with the other accelerators used to prepare the beams for LEP. During the initial running of LEP only the even numbered points had experiments in position, so collisions were only allowed to occur at these points. Later, smaller experiments were added at some of the odd numbered points which then had collisions.

2.2 The apparatus

The ALEPH experimental apparatus is situated at interaction point 4 on the LEP ring. At this point the LEP beam pipe is 137 m below the surface. The apparatus is set up in an underground cavern around this interaction point. However, much

Figure 2.2: *Layout of the ALEPH detector.*

of the support equipment such as gas storage and the experiment's control room are on the surface above the cavern.

The coordinate system used to describe the layout of the various parts of ALEPH and to describe events in ALEPH takes a horizontal line pointing toward a vertical line drawn though LEP's centre as its x axis. The z axis is defined by the e^- direction. The y axis is orthogonal to both of these axes and points upward. Events can also be described by cylindrical and spherical coordinate systems and these are related to the cartesian system by the standard conventions.

As ALEPH has been built to study e^+e^- interactions, which gives showers of particles in all directions, the detector has been designed to cover as much of the solid angle around the interaction point as possible. To get maximal information on each particle ALEPH is in fact a collection of different subdetectors that measure different properties of the particles. A quick overview of these subdetectors is given in this section. More detailed descriptions of ALEPH have been published elsewhere[2][3].

The subdetectors that make up ALEPH must be coordinated to work together. First they must know when to record a physics event, and secondly all their data must be brought together and stored ready for analysis. These two tasks are done by the trigger and data acquisition systems respectively.

The components of the ALEPH detector are described in the following subsections. The description starts from the beam pipe and works radially outwards to the muon detectors, and then along the beam pipe from the SATR to the BCAL. The Trigger and Data Acquisition systems are described in the next sections. The general layout of the apparatus is shown in Figure 2.2

2.2.1 VDET - Vertex DETector

The VDET is a silicon microstrip device which is designed to help track resolution and vertex finding around the interaction point. During the 1989 and 1990 running periods it was in a developmental stage.

The VDET is built up of silicon wafers. Each wafer has a longitudinal set of microstrips down one side, and a transverse set on the other side. This allows position detection in both r-ϕ and z directions. Four wafers are bonded together longitudinally to form a module. These modules are then placed in 2 concentric layers around the beam pipe at the interaction point. There are 12 modules in the inner layer and 15 in the outer layer.

2.2.2 ITC - Inner Tracking Chamber

The ITC is designed to give tracking information for charged particles close to the interaction point, and also to provide tracking information to the first level of the trigger.

The ITC is a cylindrical multiwire drift chamber. It contains 960 sense wires to measure the position of tracks in the chamber. The tracks are reconstructed from coordinates calculated from the sense wire output. The r-ϕ position of each coordinate can be calculated from the drift time for the ionization to reach the sense wire, and the position of the sense wire. This method has an average accuracy of 150 μm per point. The z coordinate is found by measuring the difference in arrival time for the signal pulse to reach either end of the sense wire (see Chapter 3).

2.2.3 TPC - Time Projection Chamber

The TPC is the main tracking detector for ALEPH. The aim is for it to provide accurate momentum measurements, good two track separation and measure the particles' dE/dx.

The central part of the TPC is a large cylindrical gas volume with multiwire proportional drift chambers at either end. In the middle of the cylinder is a central membrane which is kept at -26 kV (see Figure 2.3). This, along with the end-plates which are kept at 0 V, is used to create a longitudinal drift field for electrons. Each end-plate supports 18 multiwire chambers which are known as sectors. These are made up of three wire layers: one for gating; one as a

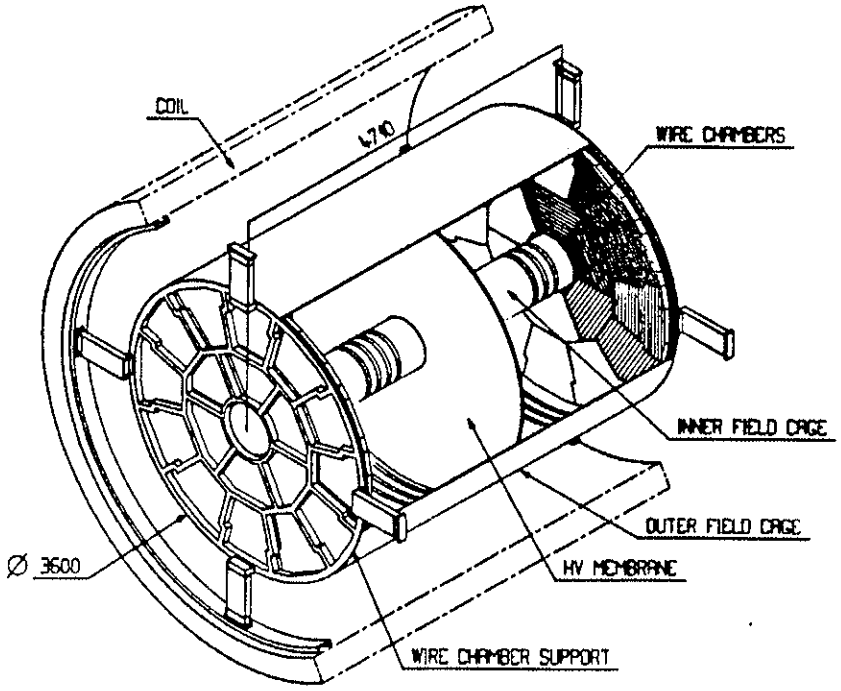

Figure 2.3: *Cutaway view of the TPC.*

cathode and one as sense wires. On the inside wall of each end-plate is a plane of cathode pads arranged to form rings around the beam pipe. The edges of the outer sectors have a 'zigzag' geometry to reduce the amount of a track that can be lost by passing over a gap between sectors

Like the ITC, the TPC reconstructs tracks from sets of coordinates. The r-ϕ coordinates are measured by finding clusters of ionization on the cathode pads and then using the pad's position to determine the coordinate. The resolution of this coordinate is dependent on many variables but the main effect is due to the pad crossing angle. With a 0° pad crossing angle, i.e. a radial track, the r-ϕ resolution is 160 μm; at 10° it is 400 μm. The z coordinate is simply found by measuring the time that it takes the ionization to reach the end-plates after a beam crossing. The variation in resolution in z is mainly dependent on the track's θ: at 90° it is 0.7 mm; at 20° it is 2.3 mm.

The charge deposited on the sense wires in the end-plates can be used to

calculate the dE/dx energy loss of a particle. This can help with particle identification (see Subsection 6.1.3). The dE/dx resolution is found to be 4.5% for tracks with 280 wire samples.

Operating the TPC in a magnetic field (see Subsection 2.2.5) causes the charged particles' tracks to curve. The curvature is dependent on the particle's momentum. Thus its momentum can be measured. The momentum resolution is found to be[4]

$$\frac{\Delta p}{p^2} = 1.2 \times 10^{-3} \frac{c}{\mathrm{GeV}}$$

for the TPC alone and

$$\frac{\Delta p}{p^2} = 0.8 \times 10^{-3} \frac{c}{\mathrm{GeV}}$$

when the ITC is included in the tracking.

2.2.4 ECAL - Electromagnetic CALorimeter

The ECAL is built to provide an accurate measurement of electron and photon energies and to help to distinguish electrons from pions. It also provides information to the trigger.

The ECAL is constructed in three independent sections, a single cylindrical barrel and two circular end-caps. The barrel is built of 12 separate, but identical, modules. Each of the barrel modules contains 45 lead sheets of either 2 or 4 mm thickness. Between these sheets are anode wire planes and planes of cathode pads. The geometry of the pads is designed such that they form 'towers' that project towards the interaction point, and have an area of about 3 x 3 cm^2, which is the approximate size of an electromagnetic shower. Therefore an electromagnetic shower should be contained within four adjacent towers. Each end-cap is made of 12 petals. These petals are of a similar design to the barrel modules with changes dictated by their different shape and attitude.

The pads in the towers are internally connected so that they are read out in three separate 'stacks'. Working outwards from the beam pipe these are 4, 9 and 9 radiation lengths deep. The energy can be calculated from the amount of

the deposited charge. The ECAL is found to have a resolution of

$$\frac{\Delta E}{E} = 1.7\% + \frac{19\%}{\sqrt{E/\mathrm{GeV}}}$$

for the pads, and

$$\frac{\Delta E}{E} = 1.6\% + \frac{17\%}{\sqrt{E/\mathrm{GeV}}}$$

for the energy when measured from the anode wire readout.

2.2.5 The superconducting coil

The superconducting coil surrounds the VDET, ITC, TPC and ECAL. It is built to give a uniform 1.5 T magnetic field parallel to the beam axis. It is kept as thin as possible so as to minimize the effect of its material on particles passing though it.

The superconducting coil is actually made up of three separate coils, a main coil and two compensating coils, one at either end of the main coil. The main coil is usually run at around 5000 A to give the 1.5 T field. The compensating coils are adjusted to remove the effects of inhomogeneities in the iron yoke of the HCAL, and thus give the uniform field to a level of 0.2%.

2.2.6 HCAL - Hadron CALorimeter and muon detectors

The iron return yoke of the magnet, which is outside the superconducting coil, has been instrumented to provide a hadronic calorimeter. The HCAL absorbs virtually all the hadrons produced by Z^0 decays, so only muons penetrate it. Outside the HCAL are the muon detectors.

Like the ECAL, the HCAL has three separate sections, a barrel and two end-caps. The barrel is again divided into 12 modules. These are made up of 22 layers of a 5 cm iron sheet and 1 cm streamer tubes, with a final 10 cm iron sheet after the last layer of tubes. This represents a total of about 7.2 interaction lengths. To avoid losing particles these modules are offset by 32.7 mrad in ϕ with respect to the ECAL modules. This means particles passing though the gaps between

ECAL modules will be observed in the HCAL. On one side of the streamer tube there are copper pads, which are arranged to form towers projecting towards the interaction point. On the other side of the streamers are aluminium strips running the length of the module in z. The end-caps of the HCAL are divided into six modules, which again have copper pads in the tower geometry, along with aluminium strips. One point to note about the end-cap modules is that only the section inside the barrel modules has the full 22 planes of iron and streamer tubes. The sections that overlap with the end of the barrel only have 16 planes (see Figure 2.2).

The HCAL is read out by three separate methods. The pads are read out individually and are used to measure the energy released into the calorimeter. The aluminium strips record whether there has been none, or at least one hit along that strip. This is often referred to as the digital readout and is important for muon identification (see Subsection 6.1.4). The wires are read out to give a measure of how much energy has been released in a given plane and are also used for triggering. The HCAL has an energy resolution of

$$\frac{\Delta E}{E} = \frac{0.84}{\sqrt{E/\mathrm{GeV}}} \ .$$

Outside the HCAL are two layers of muon detectors. Each muon detector is made up of a double layer of streamer tubes. On one side of these tubes are strips running parallel to the streamer wires (the x-strips). On the other side there are orthogonal strips (the y-strips). The two layers in a detector are offset to each other by 5 mm for the x-strips and 6 mm for the y-strips to improve point resolution.

2.2.7 SATR - Small Angle TRacker

The SATR is one of the luminosity monitors used on ALEPH. It is used in conjunction with the LCAL to give an accurate determination of the luminosity seen by ALEPH.

The SATR is made up from 144 sectors, each covering a 45° arc in the $r - \phi$

plane, and the complete detector covers the polar angles between 40 and 90 mrad at either end of ALEPH . Each sector is made up from 14 square brass cathode tubes glued to a 1 mm PCB. The PCB also supports the 25 μm wires which forms an anode inside each tube. The SATR's main objective is to detect tracks in bhabha events and measure their position. This means that the tracking algorithm from these tracks can use the interaction point as a constraint to the fit. The performance of the chamber using this method is found to be

$$\begin{aligned} \sigma_\phi &= 4.5 \text{ mrad} \\ \sigma_\theta &= 0.08 \text{ mrad} \ . \end{aligned}$$

2.2.8 LCAL - Luminosity CALorimeter

Sitting behind the SATR, the LCAL is used to measure the energies of the bhabha electrons that have polar angles between 45 and 155 mrad.

The construction of the LCAL is very similar to that of the ECAL, and so are the readout electronics. The basic design is 38 lead sheets which sandwich wire proportional tubes. Again there are cathode pads next to the tubes which are arranged to form towers projecting towards the interaction point.

In the case of the LCAL the towers are spit into three readout stacks of 4.8, 10.6, and 9.3 radiation lengths. This gives a energy resolution of

$$\frac{\Delta E}{E} = 1.4\% + \frac{20\%}{\sqrt{E/\text{GeV}}}$$

and a position resolution of

$$\sigma_x = \sigma_y = 1.4 \text{ mm} \ .$$

When the LCAL is used in conjunction with the SATR they cover the polar angles between 45 and 90 mrad. This leads to a bhabha rate approximately equal to the Z^0 rate when running at the Z^0 peak. The fractional error on the luminosity measurement using these two subdetectors is 0.7%[5].

2.2.9 BCAL - Bhabha CALorimeter

The BCAL is designed to provide an online measurement of the luminosity. The SATR and LCAL are not able to do this precisely due to the low rate of events seen by this pair. The BCAL rate is about twenty times higher than that seen in the main luminosity monitors. The BCAL luminosity measurement can be used to measure relative luminosity rates, but it has too large a systematic uncertainty to be of any use in an absolute measurement.

The BCAL is simply four rectangular modules that are fixed onto either side of the beam pipe in the $x - z$ plane just beyond the final focusing magnets of LEP. Each modules contains a sandwich of tungsten and planes of scintillator, with a single plane of silicon strips after the 4th tungsten layer.

The energies of incident particles are measured by photomultiplier tubes that are attached to the scintillator. The measured energy is dependent on where the incident particle hit. This is determined by the silicon microstrips. By requiring a coincidence between the two modules on opposite sides of the interaction point, the efficiency of the BCAL is found to be around 75%.

2.3 The Trigger

The trigger system must be able to distinguish whether a useful physics event has occurred at any given beam crossing. LEP was designed to initially produce Z^0s at a rate of about 1 Hz. The two beams cross at a rate of 44 kHz, so obviously there would not be a useful event at each beam crossing. As it takes several milliseconds to read out the full detector, reading out after every possible beam crossing would cause many of the following beam crossings to be needlessly lost. To deal with this problem the trigger has been built in three stages. Level 1 and Level 2 (the first and second decision making stages) are implemented as programmable hardware, and count as separate subdetectors. After the second level of the trigger has decided that the current event is worth recording (known as a 'Level 2 YES') all the subdetectors are read out. The third level of the

trigger is implemented in the data acquisition system and only takes effect after readout has been completed. This final level uses an analysis program, which is running on parallel processors, to decide whether or not to record the event.

2.3.1 XLV1 - LeVel 1 trigger

The first level of the trigger is designed to reduce the event rate of ALEPH from the LEP beam crossing rate of 44 kHz to around 500 Hz. To this end it takes simple pieces of data from the ITC, HCAL, ECAL and LCAL and has to make a decision whether there is a physics event present in under 5 μs. This means that if a beam crossing is rejected as containing no interesting physics event the next beam crossing is not missed.

The Level 1 decision can be roughly divided into two parts: luminosity and non-luminosity triggers. The non-luminosity trigger regards ALEPH as 60 segments that are created by dividing the apparatus up both azimuthally and by polar angle. Each segment contains a section of the ECAL and HCAL as well as covering an area of both tracking chambers. The principles of the trigger logic are shown in Figure 2.4. Analog signals are taken from areas of each calorimeter that correspond to each segment and combined to give an overall signal for that calorimeter in that segment. This overall signal is then passed through four discriminators set at different levels to produce a set of YES/NO logical signals. For offline analysis the signal is digitized and can be read out with the rest of the subdetectors. The calorimeter signals are then combined with the ITC track information for each segment to give a trigger decision. This decision can be programmed depending on the physics requirements. For instance, for a muon trigger the HCAL towers in that segment must pass the lowest discriminator cut, the HCAL wires must pass the third highest cut, and there must be an ITC track in that segment.

The luminosity trigger has a similar basis, in that analog signals from the LCAL towers are summed and put through discriminators and then put through a trigger logic. However in this decision there is no need for tracking information.

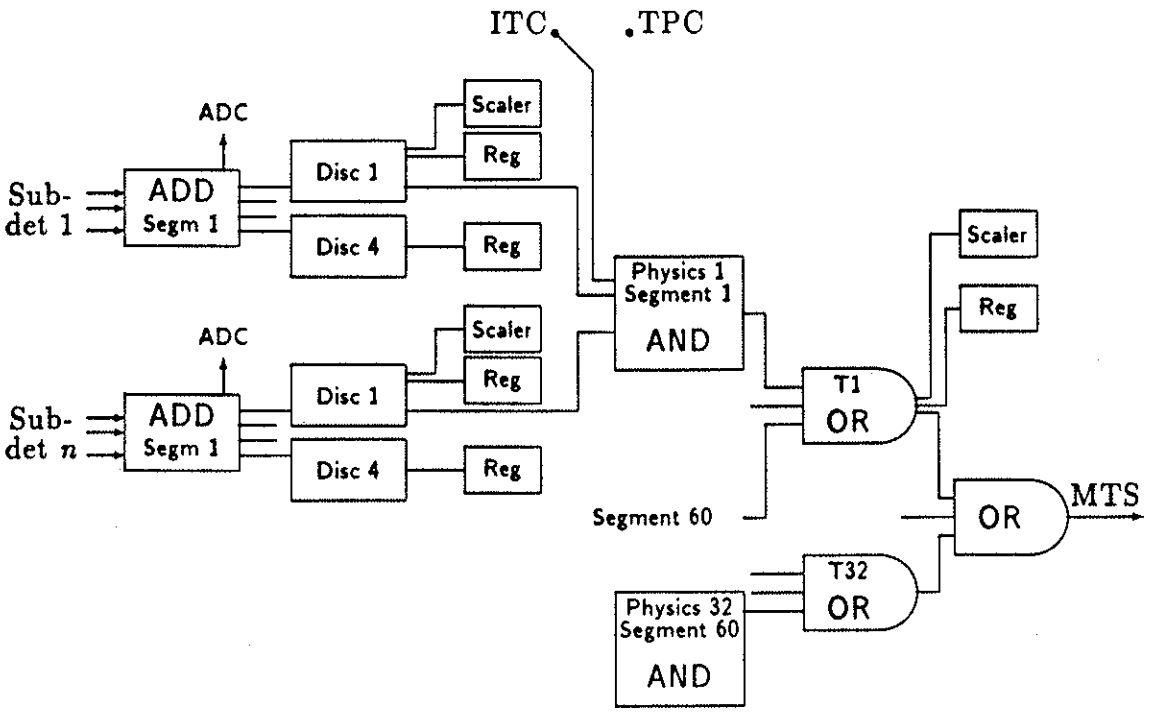

Figure 2.4: *Principle of the Level 1 and Level 2 triggers. The switch at the top of the figure is set to process the Level 1 decision. It is changed to the TPC to process a Level 2 decision.*

As far as this trigger is concerned the LCAL represents 24 more segments. This gives a total of 84 segments in the Level 1 trigger.

All the segments' trigger decisions are then ORed to give a final YES/NO answer, which is passed onto the Main Trigger Supervision (MTS). If a 'Level 1 NO' is generated all subdetectors are prepared for the next beam crossing. If a 'Level 1 YES' is generated the MTS then initiates the Level 2 trigger process.

2.3.2 YLV2 - LeVel 2 trigger

The trigger's second level is designed to reduce the Level 1 event rate to around 10 Hz. It does this by replacing the ITC track information in the trigger logic with track information obtained from the Level 2 track processors.

The Level 2 processors are designed to detect tracks in the TPC originating

from the interaction point. To be able to do this the ionization in the TPC must be allowed to drift to the end-plates. This takes about 50 μs, i.e. covering the next two beam crossings, hence the need for a Level 1 YES first. As the ionization reaches the end-plates it is detected on special trigger pads that are in between the normal TPC pads. The arrival time and pad radius of each 'hit' allows the θ of the hit to be generated and then the hit is assigned to a given 'cell'. Each cell corresponds to a selected range of θ values. For a track originating at the interaction point all its hits will be in one cell. Thus the Level 2 processors can check each cell and see if there is more than a given number of hits in it. If there are, then a track is said to exist in that cell.

This tracking information is now put into the trigger logic replacing the ITC information, and the trigger decision evaluated again. If a 'Level 2 NO' is generated then all the subdetectors are reset. If a 'Level 2 YES' is generated then all subdetectors are read out by the data acquisition system.

2.4 The data acquisition

To readout the detector the data acquisition system has been built in a tree structure. Each section of the detector, which may be a complete subdetector or just a part of one, is read out into a single processor. This processor in turn may be read out by another processor which is higher up the readout tree and reads out a number of the lower processors. Each processor may perform data reduction such as zero suppression and online calibrations, and it also formats the data ready for the next processor. At the top of each subdetector's tree is an Event Builder (EB) which collects all the data from that subdetector's lower processors. From here the data is read out into the Main Event Builder (MEB) which passes the complete event onto one of the available Level 3 processors. The Level 3 trigger does some simple pattern recognition on the data to decided if it may contain a useful physics event. If Level 3 decides this is a useful event the data is then written to a file on an online VAX cluster disk.

The file containing the data is eventually closed for one of the following reasons:

- the size limit on the tape which is going to be used to store this file has been reached;
- some aspect of the detector has changed, e.g. a subdetector is no longer being read out;
- the running conditions of LEP have changed, e.g. a new fill is started, or the background rate has significantly changed.

At this point a new file is opened so data taking may continue, and the closed file is copied to tape for permanent storage. Each complete file is known as a 'run'. Each run has its own unique run number, which is given out sequentially as data are taken.

2.5 Event reconstruction

After the data have been recorded the events need to be reconstructed, e.g. space points in the TPC have to be constructed and joined to find the tracks of the particles. This can be done any time after the data have been taken. In ALEPH, however, it has been decided that this should be done as soon as the data have been recorded onto tape. This not only allows analysis of the data to start as soon as possible, but it also allows the behaviour of the detector to be seen while data taking is still in progress and adjustments can then be made if they are necessary.

As soon as the run file has been copied to tape the disk it is stored on is dismounted from the online computer cluster and mounted on the reconstruction cluster, which is known as Falcon. The file is then copied onto Falcon's own disk and the original disk returned to the online cluster.

Falcon does a primary scan of the data file and splits it up into 12 sections. Each section is then sent to one of the 12 VaxStation 3200s which, along with the

boot node, make up the Falcon cluster. Each VaxStation then runs the standard ALEPH reconstruction program, known as JULIA, over its own section of the data and creates a reconstructed data file. When all VaxStations have done this the 12 reconstructed data files are merged and written onto a POT (Production Output Tape). After this the full reconstructed run is sent over a data network to CERN's central IBM where it is written to disk and tape ready for analysis. Data tapes for other home institutes are written automatically by the IBM once the data are received.

2.6 Run quality

Each run that is recorded, reconstructed and stored by ALEPH is assigned a quality flag that indicates how good that data is for physics analysis. There are three possible flags[6]:

PERF: All parts of ALEPH were working and LEP's physics conditions were good. Data with this flag should be able to be used for all physics work.

MAYB: Either part of ALEPH was not working correctly, or LEP's physics conditions were bad, e.g. there were high backgrounds. Data with this flag maybe useful for physics, but the problem should be checked to see if it influences the analysis being considered.

DUCK: There was a major problem with the data taking and so this run should be ignored for any physics analysis.

The decision on a run's quality is usually made by the Run Managers shortly after the run has been taken. However it is sometimes possible to recover from errors that have occurred by reprocessing the data and then the new data can be given a different quality flag.

Chapter 3

The ITC z coordinate

As discussed in Chapter 2 the ITC is designed to produce trigger information as well as track coordinates. To date the trigger processing is done using just $r-\phi$ information. This task was done by the $r-\phi$ processor. However it is planned to increase the decision-making power of the ITC trigger by introducing the Space Point processor which uses information about z coordinates as well as $r-\phi$. For the Space Point processor to work efficiently the z readout must be understood and a non-linearity, known as the S-bend, quantified. This chapter explains how the S-bend parameters are determined and other features of the readout understood.

3.1 ITC trigger

3.1.1 Sense wire readout

The 960 sense wires in the ITC are set out in 8 concentric cylinders, or layers. These layers are numbered from the centre out. There are 96 wires in each of the inner four layers, and 144 in each of the outer four. Each sense wire is surrounded by 6 field wires of which 4 are shared with its neighbours in the same layer. A schematic of the wire layout is shown in Figure 3.1. Each 'cell' around a sense wire is approximately 1 cm in diameter. The sense wires are held at about 2.0 kV while the field wires are earthed. The calibration feed wire is used to send a pulse

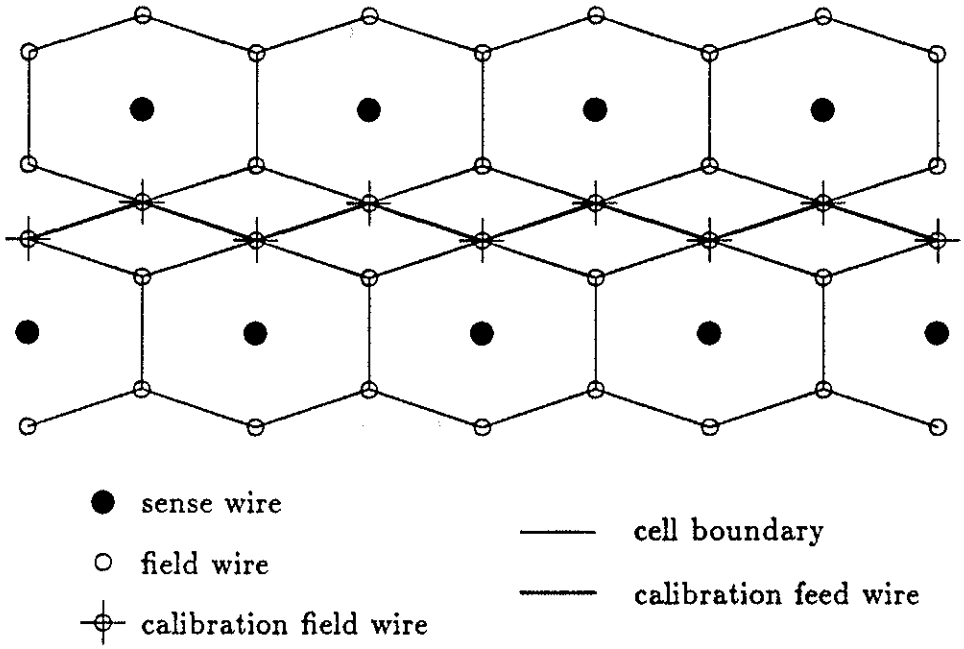

Figure 3.1: *Schematic layout of a bilayer of sense wires in the ITC.*

down all the calibration field wires. This pulse will simulate a hit at $z = 0$ and is used to calibrate the z readout.

Any signal on a sense wire is measured at both ends by a pre-amp. The output of the pre-amp is then sent to an 'AZ board' in the ITC counting rooms. The AZ board amplifies, discriminates and does a time expansion (explained later) on the incoming signal. The outputs of the AZ board are as follows:

- a pulse to measure the drift time, i.e. the time between the beams crossing and the signal reaching the wire. This is sent to a 4299 LeCroy TDC for digitizing and recording;

- an ON/OFF hit 'latch' which is used by the $r - \phi$ processor to decide if there are any radial tracks in the ITC;

- a pulse indicating the position of the hit along the wire. This is sent to the

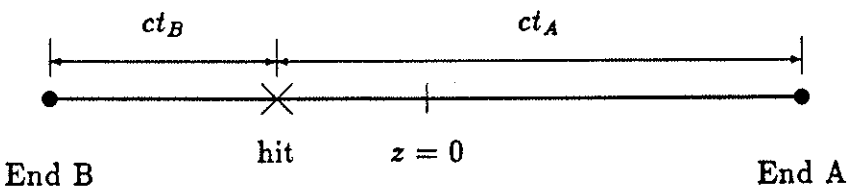

$$
\begin{aligned}
\Delta t &= \text{difference in time of arrival} \\
&= t_B - t_A \\
t &= \text{time of propagation} \\
c &= \text{speed of propagation} \\
z &= \tfrac{1}{2}(ct_B - ct_A) \\
&= \tfrac{c}{2}\Delta t
\end{aligned}
$$

Figure 3.2: *Calculation of the z coordinate from the difference in arrival times, assuming the speed of propagation is constant.*

Space Point processor[1] which tests for tracks that pass through the beam crossing point. This pulse is also sent to a 1879 LeCroy TDC for digitizing and recording.

The last output is created by taking the difference of the arrival time at each end of the wire. This difference is expanded by a set amount, known as the expansion factor or slope, and a constant term is added, known as the offset. Figure 3.2 shows how the z coordinate can be derived from the time difference. The time expansion is calibrated so that all the pulses corresponding to the hits from a track that passed through the interaction point occur at the same time. Tracks that do not pass through this point will have their pulses spread over a period of time. This idea is shown schematically in Figure 3.3.

[1]Only one of the $r - \phi$ and Space Point processors will be installed at any given time.

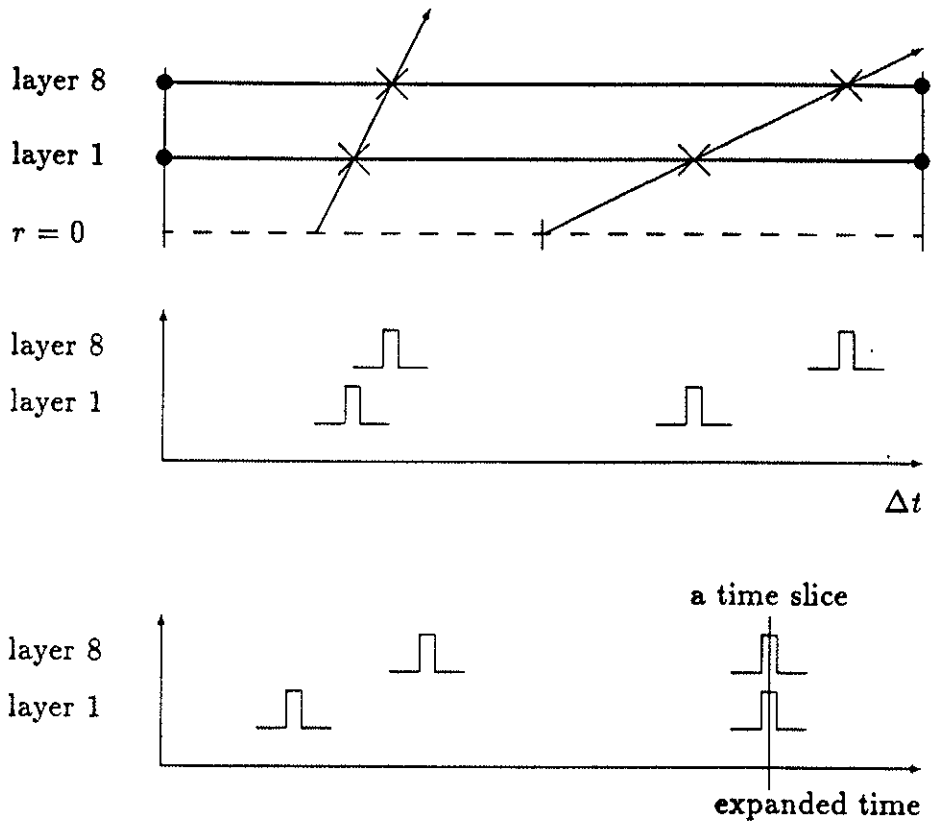

Figure 3.3: *Schematic showing the effect of time expansion on z hits. Pulses generated by a track passing through the interaction point will all occur at the same time. A track not passing through this point will have its pulses spread over a period of time.*

3.1.2 The $r-\phi$ processor

The idea behind the $r-\phi$ processor is to find radial patterns of hits which indicate that there is a track coming from the $r = 0$ axis. To do this sets of wires with similar ϕ values are grouped together in sets called masks. All the hits from a radial track with $p > 1$ GeV/c should appear within a single mask. To avoid losing tracks between masks, the masks overlap so a wire will appear in more than one mask. To determine whether the hit pattern of a mask indicates a track the ON/OFF latches for each wire in the mask are used to create a 14 bit address. This address can then be used to read a RAM location whose contents will flag whether that particular pattern of hits represents a track.

3.1.3 The Space Point processor

The Space Point processor is based on a similar principle to that of the $r-\phi$ processor. The main change is that instead of producing a single address from the ON/OFF latches, a series of addresses are created by looking at the third output of the AZ boards at various points in time. This is known as time slicing the output. As all the pulses from a track through the interaction point occur at the same time they will all be included in a single address. This address will be the same as the one the $r-\phi$ processor would have generated.

A radial track that does not pass through the origin will still produce a 'valid' address, i.e. one that implies a track, in the $r-\phi$ processor. However in the Space Point processor the pulses corresponding to the track's hits are spread over a period of time and will therefore be included in different addresses. This means that they will no longer create a valid address.

3.2 Analysing the z readout

3.2.1 Track selection

To study the z readout it is necessary to know the actual z coordinate of each ITC hit. As the TPC has a track resolution of a few 100 μm in z and the expected ITC resolution is a few centimetres it is possible to use track information from the TPC to find the z coordinate of ITC hits. This is done by finding the z coordinate of the intersection of the track's helix with a cylinder whose radius is that of the wire which is hit. To make the track to hit association as good as possible and to minimise the chance of multiple hits on a wire, only events with one or two charged tracks are used in this study. Moreover, as the Space Point processor is only interested in tracks passing through the beam crossing point, a track is only used if it passes all of the following requirements:

$$\begin{aligned} \text{Momentum} &\geq 0.3 \text{ GeV}/c \\ \chi^2 \text{ per degree of freedom} &\leq 3.0 \\ \text{Number of hits in ITC} &\geq 4 \\ \text{Number of hits in TPC} &\geq 4 \\ d_0 &< 0.5 \text{ cm} \\ z_0 &< 5.0 \text{ cm} \ , \end{aligned}$$

where d_0 is the $r - \phi$ distance of the track's closest approach to the beam axis and z_0 is the z coordinate of this point.

The data used in this chapter comes from all the PERF and MAYB runs taken by ALEPH during 1990.

3.2.2 Preparing the z TDC output

By looking at the spread of TDC counts for a selected range of z on a layer (Figure 3.4 shows two example distributions) it can be seen that there are a number of hits in the tails. These indicate that there are some hits which have a bad $z \rightarrow$ TDC count relationship. These hits provide no useful information about

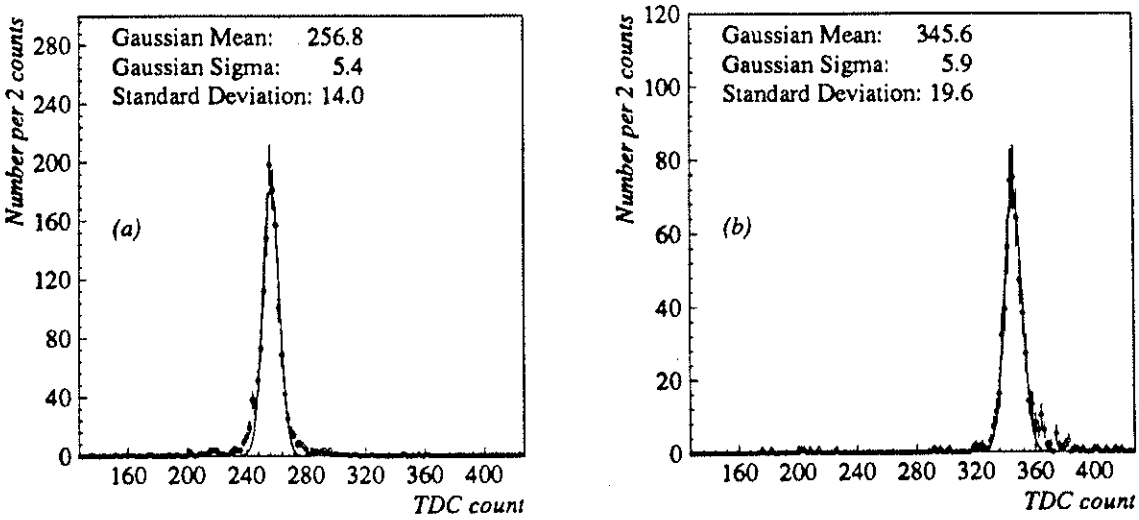

Figure 3.4: *Spread of the raw output of the z TDC's (a) for* $19.5 < z < 20.5$ *in layer 1, and (b) for* $-80.5 < z < -79.5$ *in layer 8.*

the track. Therefore, as this 'noise' will hinder the evaluation of the S-bend, an algorithm has been developed to remove them.

The algorithm works on the principle that the TDC values on a given track should all be the same since the track is required to have come from the origin. The mean and standard deviation of all the TDC counts on the track are calculated. If the standard deviation is greater than a certain limit the track is taken to have at least one bad z hit on it. If this is the case then the TDC value furthest from the mean is removed from the track and the mean and standard deviation recalculated. This process is repeated until the standard deviation is within the limit. The optimum limit was found to be around fifteen. This removes obvious bad hits but does not stop a track having some hits that were of the order of 20 counts away from the mean. If a track has fewer than 4 ITC hits remaining after it has been 'cleaned' then it is rejected entirely. The effect of cleaning on the TDC spread is shown in Figure 3.5 (compare this with Figure 3.4). The Gaussian fit is done with each bin having an equal weight. This means that highly populated 'signal' bins are emphasised. It can be seen that the signal is unaffected by this

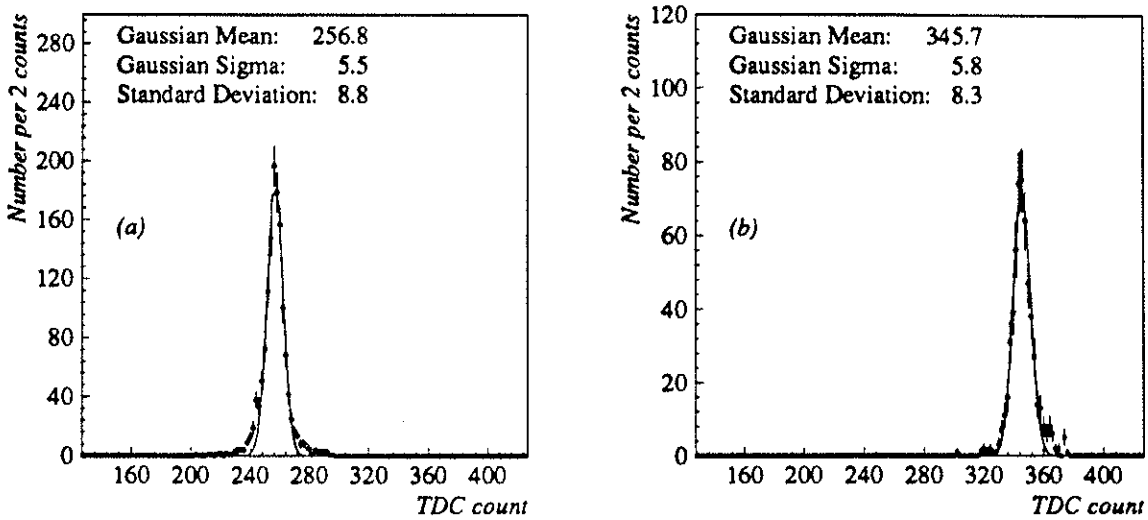

Figure 3.5: *Spread of the output of the z TDC's after removing 'bad' hits (a) for* $19.5 < z < 20.5$ *in layer 1, and (b) for* $-80.5 < z < -79.5$ *in layer 8.*

cleaning. However, the large drop in the standard deviation shows that the long tails have been removed.

Information on the calibration of each wire can be obtained by performing straight line fits to the z coordinates versus TDC values. The $z \rightarrow$TDC count relationship is approximately linear but with a small, roughly sinusoidal component – the so called 'S-Bend'. The S-bend is caused by reflections at either end of the wire. The reflections are due to a mismatch on the transmission line as the pulses goes through the end-plates. These reflections cause a change in the leading edge of the pulses and this affects the timing of the discriminated signal, giving rise to a non-linear relationship.

The S-Bend implies that the fitted slope is dependent on the range of z being used. However, provided the range of z used is symmetric about $z = 0$, then the S-bend's effects on the offset will cancel out and the fitted offset is simply the TDC count representing $z = 0$ on that wire. The calibration should ensure that the offsets are the same for all wires.

The results of the fits for the offsets for layer 1 are shown in Figure 3.6. It can

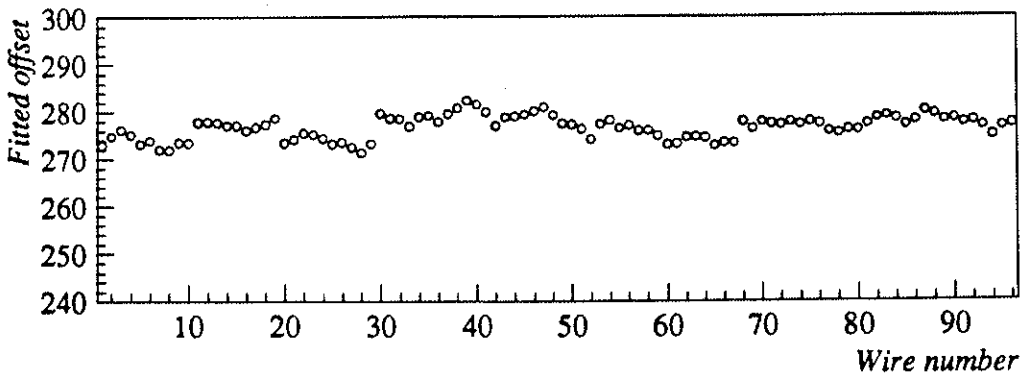

Figure 3.6: *Fitted offset for all wires in layer 1.*

be seen that some groups of wires have offsets significantly shifted with respect to the mean offset. This structure is seen in all layers and is found to be directly correlated with individual TDC modules. (In fact when modules were moved around in the readout the offset shift moved with them, thus confirming this shift is a feature of the TDC.) The mean offset for each TDC module can be measured and then used to adjust the individual TDC values of wires in that module. When this correction is included, the widths of the TDC spreads, for a given z, decrease by approximately 20%. For instance the average sigma of the fitted Gaussian for layer 8 drops from 5.8 for the 'cleaned' data to 4.8 for 'cleaned' and 'shifted' data. An example of the TDC spreads after both cleaning and shifting are shown in Figure 3.7.

3.2.3 Measuring the S-bend

Having prepared the z TDC data sample it is now possible to measure the non-linearity. This manifests itself as a difference between the actual $z \rightarrow \Delta t$ relationship and that given by the simple linear relationship summarised in Figure 3.2. If Δz is the difference between these two relationships, it can be calculated using

$$\Delta z = z_{\text{hit}} - (\mathcal{T}_0 - \mathcal{T})W \cdot K\frac{c}{2}$$

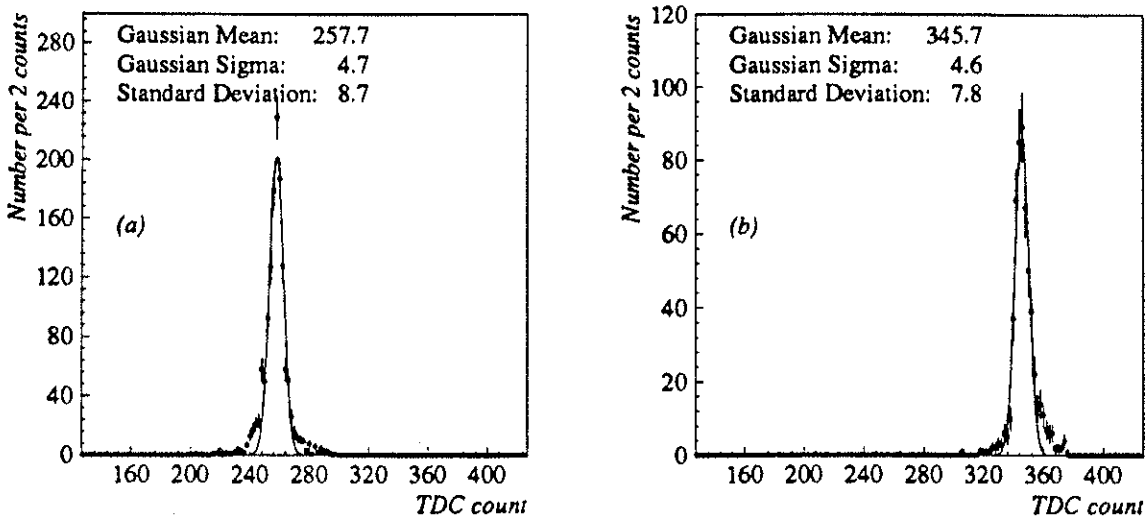

Figure 3.7: *Spread of the output of the z TDC's after removing 'bad' hits and correcting for TDC module offsets (a) for* $19.5 < z < 20.5$ *in layer 1, and (b) for* $-80.5 < z < -79.5$ *in layer 8.*

where z_{hit} is the actual z coordinate of the hit, $\mathcal{T}$ is the TDC count of the hit,$\mathcal{T}_0$ the TDC count at $z = 0$, W is the bin width of the TDC in seconds, K is the inverse of the expansion factor of the layer, i.e. the contraction factor, and c is the speed of propagation, i.e the speed of light. W is normally set to be 4 ns while layer 8 has an expansion factor of 100. Therefore one TDC count on layer 8 is equivalent to 1.2 cm.

Before evaluating the S-bend it is important to remember that the track selection causes the hits to be in a finite, layer dependent, range of z which is centred around $z = 0$. The range of z for each layer for a track with $\cos(\theta) = 0.95$ is shown in Table 3.1. Also shown are the TDC counts that are equivalent to that value of z and a 'cutoff' count that is taken as 24 counts inside the equivalent count. The cutoff is a count inside which a TDC count will have unbiased contributions from higher and lower z. Outside the cutoff there will be a biased contribution due to the drop off in z hits caused by the finite z range.

Work on the test chamber of the ITC[7] showed that the non-linearity could

Layer	Radius (cm)	$\pm z$ Range (cm)	Equiv. bin (+ve)	Chosen TDC cutoff	Equiv. bin (-ve)	Chosen TDC cutoff
1	16.11	49	223	247	331	307
2	17.20	52	222	246	332	308
3	18.70	56	220	244	334	310
4	19.79	59	219	243	335	311
5	21.68	66	217	241	337	312
6	23.01	70	216	240	338	314
7	24.69	75	212	236	342	318
8	26.02	79	209	233	345	321

Table 3.1: *z cutoff, based on a track with* $\cos(\theta) = 0.95$, *and the associated TDC count, and the cutoff count.*

be approximated by a sine function with a period $L \simeq$ 160cm. Therefore, due to the limited z range being used, the S-bend period can not be measured from the data of inner layers.

The sine function used to model the S-bend is defined by three parameters:

A: which is an offset for each layer due to the fact that the calibration pulse may not be at $z = 0$, whereas the S-bend will be symmetric around this point and so may be slightly shifted with respect to $\mathcal{T}_0$;

B: which is the amplitude of the sine function;

T: which is the period of the sine function.

Both B and T are properties of the signal propagation down the wire. As the local architecture of each wire is similar, these parameters should be reasonably independent of the wire's layer.

Layer	A	B	Period (TDC)	Period T (cm)
1	0.6±0.05			
2	0.6±0.05			
3	-0.7±0.05			
4	-0.9±0.05			
5	0.5±0.05	10.3±0.6	-225±17	225
6	0.5±0.05	9.9±0.4	-192±10	204
7	-1.4±0.05	9.7±0.4	-178±10	203
8	-0.8±0.05	9.2±0.5	-170±12	205

Table 3.2: *Results of fitting for the S-Bend. Only the outer 5 layers have a large enough range in z to allow a useful measurement of B and T. Their fit was restricted to a TDC range equivalent to* $241 < \mathcal{T} < 313$ *on layer five.*

The values of the three parameters can be derived by fitting the function

$$A + B.\sin(\frac{2.\pi}{T}(\mathcal{T}_0 - \mathcal{T})W \cdot K\frac{c}{2})$$

to the Δz distribution. For every hit that gives a particular TDC value the Δz of the hit is calculated and histogrammed. The mean of a Gaussian fit to this histogram is used as the value of Δz for that TDC value. This Δz value is then used in the fit for the S-bend. The fit is done for the outer four layers and the results are shown in Figure 3.8. The range of TDC counts chosen for these four layers is equivalent to the wire length covered by $241 < \mathcal{T} < 313$ on layer five. The inner four layers were only fitted to obtain A, and so their TDC ranges were chosen to be those dictated by the TDC cutoffs in Table 3.1.

The results of the fits are summarised in Table 3.2 along with the fits to obtain A for the inner four layers. The outer three layers show good agreement for the S-band parameters. However if we superimpose the mean result of these three layers on a plot showing the full TDC range allowed for layer 8 (Figure 3.9(a))

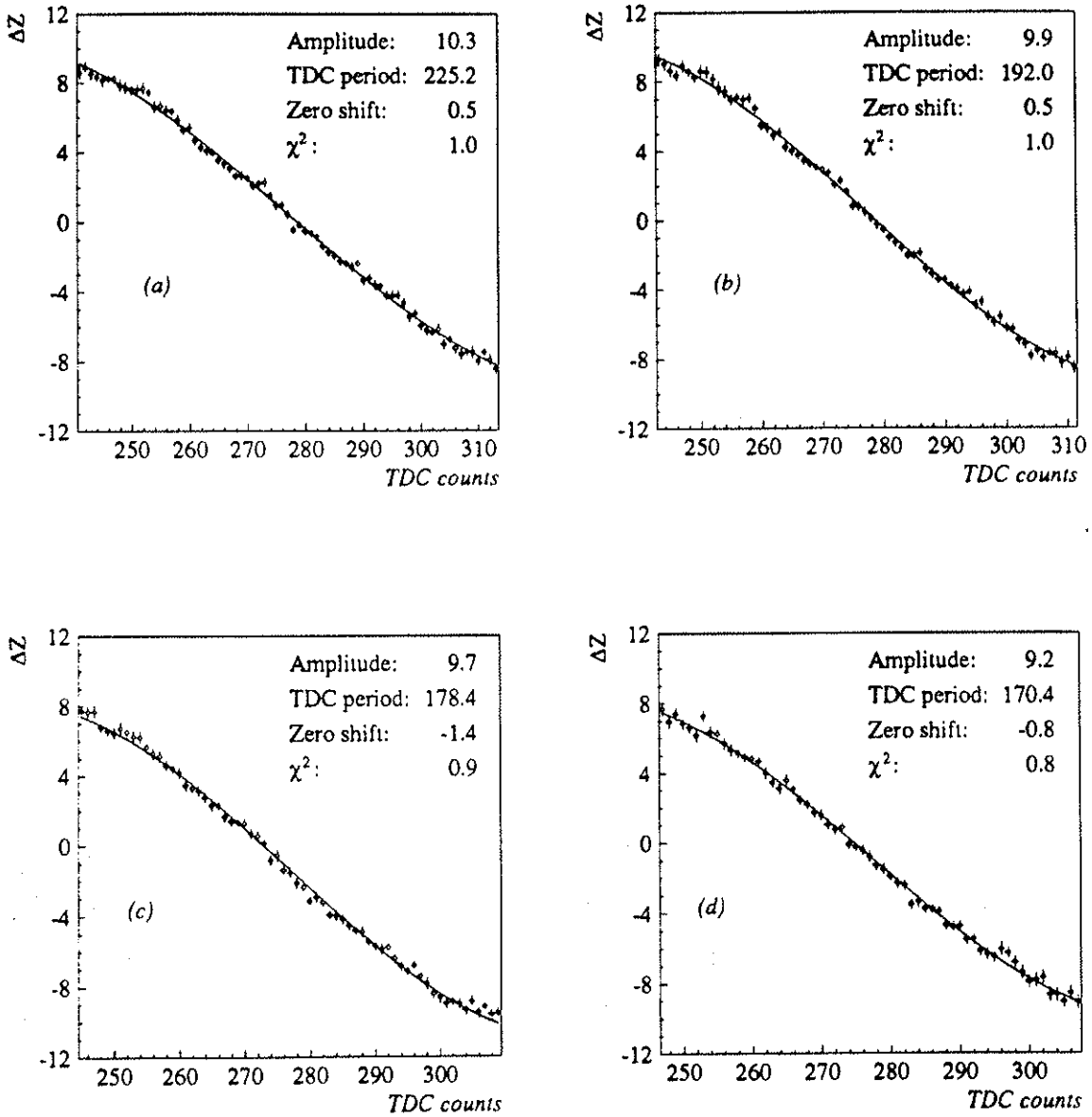

Figure 3.8: *Sine wave fits to Δz for layers (a) 5, (b) 6, (c) 7 and (d) 8.*

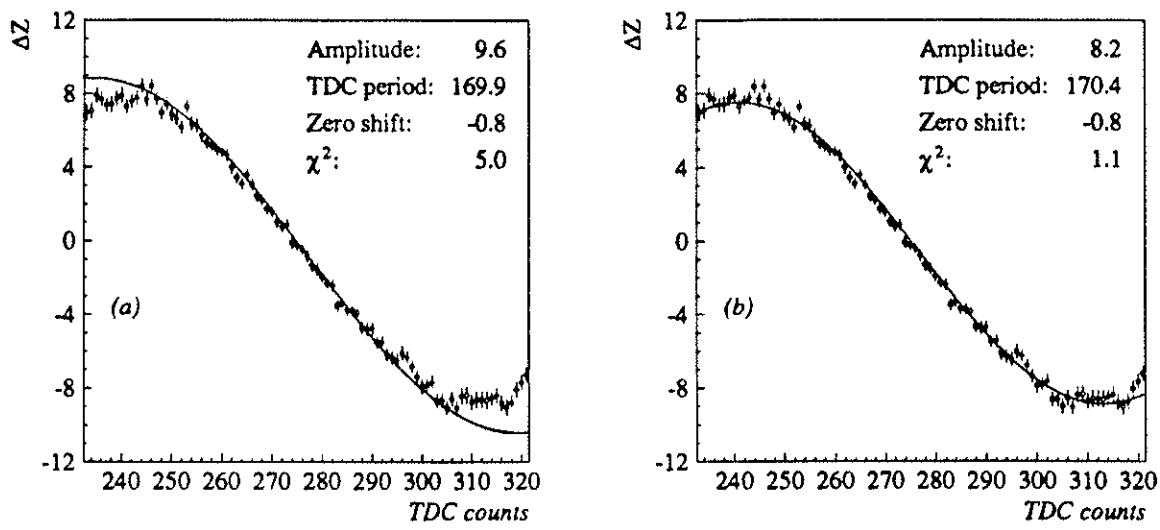

Figure 3.9: *(a) Average S-bend fit from the outer three layers superimposed on the layer 8 data. (b) S-bend fit over the full TDC range for layer 8.*

we can see that this result does not model the fall-off behaviour at large z. Therefore a good S-bend parameterisation can only be derived from a fit to the data from layer 8. This fit is shown in Figure 3.9(b). It can be seen that this still models the central region well, but now also models the fall-off. The χ^2 of this parameterisation of the S-bend with respect to each layer is shown in Figure 3.10. It can be seen that this parameterisation is not as good as an individual fit to each layer. However those individual fits have been shown not to model that behaviour outside the z range used for the fit. Therefore it is preferable to use the full layer 8 parameterisation for all layers.

Another feature in Table 3.2 to note is that A is very similar for layers in the same bilayer. This is to be expected as the calibration pulse is fed to each bilayer, rather than to each layer separately. This can be seen in Figure 3.1. The offsets for each bilayer are given in Table 3.3.

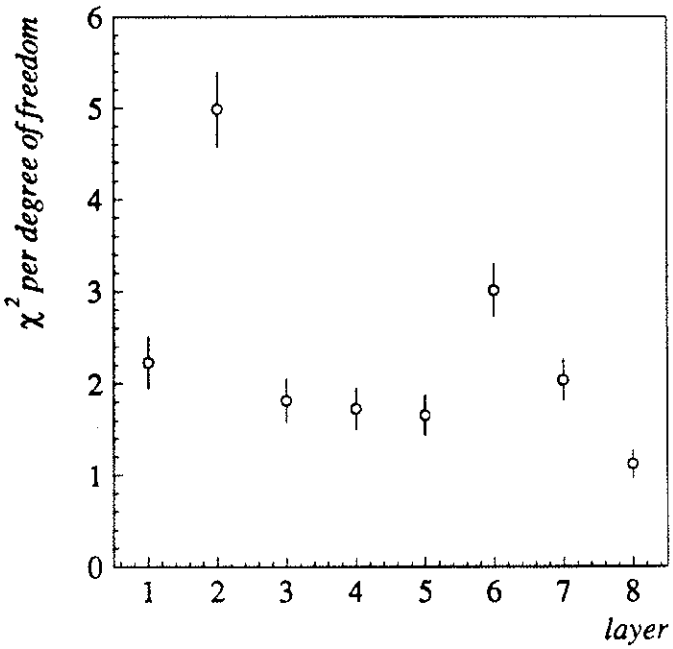

Figure 3.10: χ^2 *for the S-bend parameterisation for each layer.*

Layer	Offset (cm)
1 & 2	-0.6
3 & 4	0.8
5 & 6	-0.5
7 & 8	1.1

Table 3.3: *Offset of the calibration pulse from* $z = 0$ *for each bilayer.*

3.3 Conclusions

The z readout of the ITC has been shown to be working. It is now known that each z TDC module has a slightly different offset, and this needs to be corrected for offline when calculating the z coordinate. As the calibration of the offset is done by a single TDC, the pulses from the AZ board to the Space Point processor are correctly adjusted to be coincidental and therefore do not need to be adjusted for this feature. However, these pulses do need to be corrected to allow for the shift of the calibration pulse away from the true $z = 0$ position.

The S-bend in the ITC has been measured using the data from layer 8 and it can be reasonably modeled by a sine function with:

$$\begin{aligned} \text{Amplitude} &= 8.2 \text{ cm} \\ \text{Period} &= 173 \text{ cm} \ . \end{aligned}$$

These parameters are in general agreement with the values measured in the test chamber of the ITC, which were $B \simeq 10$ cm and $T \simeq 160$ cm.

Studies are now in progress to see how the S-bend affects the efficiency of the three dimensional processor. A prototype of which is currently being commissioned at CERN.

Chapter 4

An introduction to $B^0 - \bar{B}^0$ mixing

It is currently believed that basic physical phenomena can be described using four forces and a limited number of fundamental particles. The four forces are gravity, electromagnetism, the weak and the strong nuclear forces. As gravity is substantially weaker than the other three forces ($\sim 10^{-38}$ that of electromagnetism) it is usually ignored when looking at individual particle interactions and will not be discussed further here. Of the remaining forces, electromagnetism and the weak nuclear force have now been combined into a single framework called the Electroweak force, and the strong nuclear force is believed to be described by Quantum Chromodynamics (QCD). Together, these two theories have been tested in a large number of ways and have shown very good agreement with nature. The Electroweak theory has been so successful that it is now commonly referred to as the "Standard Model".

4.1 The Standard Model and QCD

The Standard Model is based on two types of particles, fermions with spin $\frac{1}{2}$, and bosons with spin 1. The known fermions, which are usually considered to be the particles of matter, show a repetitive structure and so are grouped in families or generations. Each generation contains four particles and their associated antiparticles. The particles are a charged and a neutral lepton, and two quarks, one with a charge of $-\frac{1}{3}$ and the other with a charge of $+\frac{2}{3}$. Apart

Leptons		Quarks	
Charge = 0	Charge = −1	Charge = $-\frac{1}{3}$	Charge = $+\frac{2}{3}$
ν_e	e	down(d)	up(u)
ν_μ	μ	strange(s)	charm(c)
ν_τ	τ	bottom(b)	top(t)

Table 4.1: *Families of particles in the Standard Model.*

from the different charges, quarks differ from leptons in another way, in that they experience the strong nuclear force whereas the leptons do not. Recent results from LEP[8] have shown that there are only three generations with light neutrinos (the neutral lepton) within the framework of the Standard Model. The members of these three families are listed in Table 4.1. Although the top quark has not yet been observed directly, it is a fundamental part of the model and has direct repercussions on $B^0 - \bar{B}^0$ mixing. In fact when ARGUS first measured significant $B_d^0 - \bar{B}_d^0$ mixing[9] it led to the prediction that the top mass had to be greater than 45 GeV/c^2[10]. The current limits on the top mass are $77 < m_t < 203$ GeV/c^2 [11][12].

The bosons in this model are usually considered to be the propagators of the forces. Their existence is rather elegantly predicted by describing the interactions of fermions in terms of gauge fields. The formal structure of these fields comes from quantum field theory. By requiring the field interactions to be invariant under certain symmetry groups, i.e. SU(2)⊗U(1) for the electroweak part and SU(3) for QCD, it is found that vector fields must be introduced to preserve the interaction's invariance. These vector fields appear to describe the bosons observed in nature. However, for the symmetry to hold in this model the vector fields must be massless, but in reality not all the observed bosons are massless. This problem is solved by introducing a scalar field with a non-vanishing vacuum expectation value, which couples to the boson and fermion fields. The inclusion of this new field moves the minimum of the interaction potential away from the

Bosons	number	force
Photon(γ)	1	electromagnetic
Z^0	1	weak nuclear
W	2	weak nuclear
Gluon	8	strong nuclear

Table 4.2: *Gauge vector bosons of the Standard Model.*

origin, thus hiding the symmetry. This behaviour generates the mass terms for the bosons and fermions. This new field is known as the Higgs boson and, like the top quark, it has not yet been directly observed. A summary of gauge vector bosons found in the standard model is given in Table 4.2

4.2 Cabibbo-Kobayashi-Maskawa mixing matrix

In the Standard Model developed from gauge theoretical symmetries there is no implicit mechanism for quark mixing which would lead to phenomena such as strange quark decay. This mechanism has to be added explicitly by postulating that the mass eigenstates are not the eigenstates of the weak force. The two different bases are related by the Cabibbo-Kobayashi-Maskawa (CKM) mixing matrix which was originally laid out for 2 generations by Cabibbo[13] and then generalised for more generations by Kobayashi and Maskawa[14]. Conventionally the up type quarks remain unchanged and the down type quarks are mixed using

$$\begin{pmatrix} d' \\ s' \\ b' \end{pmatrix} = \begin{pmatrix} V_{ud} & V_{us} & V_{ub} \\ V_{cd} & V_{cs} & V_{cb} \\ V_{td} & V_{ts} & V_{tb} \end{pmatrix} \begin{pmatrix} d \\ s \\ b \end{pmatrix} .$$

The values of each matrix element can, in principle, be measured from the relevant decays of each quark. While this is true in practice for the lighter quarks the top quark presents a problem as it has not been observed. Moreover it is expected to have a short lifetime which will make any accurate measurement

difficult. Fortunately there are other ways to evaluate the bottom row of the matrix. One method is to use the fact that the laws of transformations mean V has to be unitary. Therefore information from the other elements can be used to construct the missing values. Another way is to use indirect methods such as $B^0 - \bar{B}^0$ mixing where a virtual top quark appears in the diagrams that describe mixing (see Section 4.3).

As the CKM matrix has to be unitary this places a restriction on the number of parameters required to define it. Moreover, as it is possible to arbitrarily define the quarks' phases, the number of free parameters is further reduced. For a three generation Standard Model the matrix can be fully described by three real angles and a complex phase. The complex phase is important as it is necessary to account for CP violation. The current ranges of the elements of the CKM matrix, at a 90% confidence limit, are [1];

$$\begin{pmatrix} 0.9747 \text{ to } 0.9759 & 0.218 \text{ to } 0.224 & 0.001 \text{ to } 0.007 \\ 0.218 \text{ to } 0.224 & 0.9734 \text{ to } 0.9752 & 0.030 \text{ to } 0.058 \\ 0.003 \text{ to } 0.019 & 0.029 \text{ to } 0.058 & 0.9983 \text{ to } 0.9996 \end{pmatrix} . \qquad (4.1)$$

The first two rows are evaluated by the following means:

$|V_{ud}|$ Comparing nuclear beta decay with muon decay.

$|V_{us}|$ Analysing $K^0 \rightarrow \pi^{\mp} e^{\pm} \nu$ and $K^{\pm} \rightarrow \pi^0 e^{\pm} \nu_e$ (collectively known as K_{e3} decays).

$|V_{ub}|$ The lepton spectrum of semileptonic decays of B mesons gives a measurement of $|V_{ub}/V_{cb}|$.

$|V_{cd}|$ Neutrino and antineutrino production of charm off valence down quarks combined with the semileptonic branching fraction for charmed mesons.

$|V_{cs}|$ Comparing the measured D_{l3} decay width with the theoretical formula for $\Gamma(D \rightarrow \bar{K} e^+ \nu_e)$.

$|V_{cb}|$ Repeating the method of $|V_{cs}|$ but using the B_{l3} decay, $\bar{B} \rightarrow D l \bar{\nu}_l$.

The final row is constructed by using the unitarity constraint. For more details and references see [1].

4.3 $B^0 - \bar{B}^0$ mixing

Mixing between the neutral pseudoscalar mesons K^0 and $\bar{K}^0$ has been known about for some time. There is no reason to believe that this behaviour will not be repeated by heavier pseudoscalars such as D^0's and B^0's. Indeed the formalism necessary to describe the effects of mixing are the same. For the sake of clarity the weak interaction will be assumed to be CP invariant throughout this section. The effects of CP violation will be discussed later.

Having assumed CP invariance, the weak decays of the neutral B meson must occur from CP eigenstates. However the flavour eigenstates are not the CP eigenstates as

$$CP\,|B^0\rangle = |\bar{B}^0\rangle \quad .$$

The CP eigenstates are therefore the linear combinations

$$\begin{aligned} |B_1\rangle &= \frac{1}{\sqrt{2}}(|B^0\rangle + |\bar{B}^0\rangle) \qquad (CP = +1) \\ |B_2\rangle &= \frac{1}{\sqrt{2}}(|B^0\rangle - |\bar{B}^0\rangle) \qquad (CP = -1) \quad . \end{aligned}$$

As B_1 is unstable, its statefunction can be written as

$$|B_1(t)\rangle = e^{-(i\cdot m_1 + \Gamma_1/2)\cdot t}|B_1(0)\rangle \quad ,$$

where Γ_1 is its width and m_1 its mass. Then the statefunction of an initially pure B^0 state can be constructed by combining this equation with the equivalent one for B_2 to give

$$\begin{aligned} |B^0_{t=0}(t)\rangle &= \frac{1}{2}(e^{-(i\cdot m_1+\Gamma_1/2)\cdot t} + e^{-(i\cdot m_2+\Gamma_2/2)\cdot t})|B^0\rangle \\ &+ \frac{1}{2}(e^{-(i\cdot m_1+\Gamma_1/2)\cdot t} - e^{-(i\cdot m_2+\Gamma_2/2)\cdot t})|\bar{B}^0\rangle \quad . \end{aligned}$$

Using this, the probability of finding a B^0 at a time t later is

$$P_{B^0}(t) \equiv |\langle B^0|B^0_{t=0}(t)\rangle|^2 = \frac{1}{4}\left[e^{-\Gamma_1\cdot t} + e^{-\Gamma_2\cdot t} + 2\cdot e^{-\Gamma\cdot t}\cdot\cos(\Delta m\cdot t)\right] \quad , \quad (4.2)$$

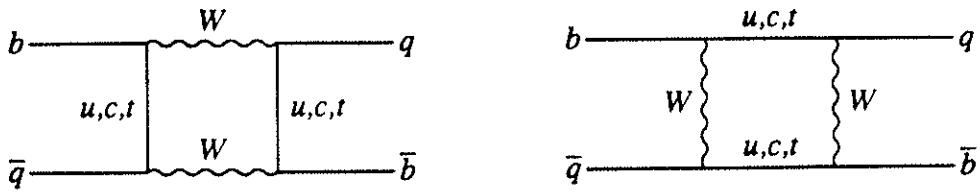

Figure 4.1: *Dominant diagrams for $B^0 - \bar{B}^0$ mixing where q can either be a down or strange quark.*

and that of finding a $\bar{B}^0$ is

$$P_{\bar{B}^0}(t) \equiv |\langle \bar{B}^0 | B^0_{t=0}(t) \rangle|^2 = \frac{1}{4}\left[e^{-\Gamma_1 \cdot t} + e^{-\Gamma_2 \cdot t} - 2 \cdot e^{-\Gamma \cdot t} \cdot \cos(\Delta m \cdot t)\right] \quad . \quad (4.3)$$

Here $\Gamma = \frac{1}{2} \cdot (\Gamma_1 + \Gamma_2)$ and $\Delta m = m_1 - m_2$. It can be seen from these equations that an initially pure B^0 state will contain some $\bar{B}^0$ at a later time, i.e. the B^0 has mixed. Present experiments do not have enough resolution to measure $B^0 - \bar{B}^0$ mixing as a function of time. Therefore only the time integrated measurement will be considered from here on.

The two diagrams that give the dominant contribution to this mixing are the 'box' diagrams shown in Figure 4.1. By considering these diagrams and the similar ones for K^0 an important difference can be seen. The $K^0 - \bar{K}^0$ mixing case in which top quarks are the internal lines is heavily suppressed as both $|V_{td}|$ and $|V_{ts}|$ are small. However in the $B^0 - \bar{B}^0$ mixing case $|V_{tb}|$ is almost unity and therefore this case is not as suppressed. In fact, due to the high mass of the top quark, this case dominates and the up and charm exchange terms can be neglected. This means that $B^0 - \bar{B}^0$ mixing can provide us with useful information about the top's components in the CKM matrix.

Evaluating the diagrams in Figure 4.1 is not trivial. One of the problems comes from the fact that the B^0 is a bound quark state so there are QCD contributions in the diagrams. The problem with QCD is that perturbation theory can not be used to evaluate its contribution as its coupling constant, α_s, is of the order of unity at B meson energies. Also the evaluation is influenced by the

unknown top quark mass. However, many of these contributions are the same for B_d^0's and B_s^0's, so that they cancel when considering the ratio x_d/x_s, where

$$x_q \equiv \frac{\Delta m}{\Gamma}$$

for a B_q^0 system. A reasonable approximation to the ratio is[15]

$$\frac{x_d}{x_s} = \frac{|V_{td}|^2}{|V_{ts}|^2} \cdot \left(\frac{f_{B_d}}{f_{B_s}}\right)^2 \quad .$$

where f_{B_q} is the decay constant for the B_q^0 meson and represents the SU(3) symmetry breaking effects of the quark masses. These decay constants for B mesons have not be measured directly as the $B \rightarrow \tau\nu_\tau, \mu\nu_\mu$ decays that are required are very rare. There are a number of theoretical predictions for f_{B_d}/f_{B_s} from QCD sum rules [16] and lattice calculations [17], but these have large errors so do not provide too much numerical information. However they do predict that $f_{B_d} < f_{B_s}$, so using the current limits on the values in the CKM matrix given in Equation 4.1

$$\frac{x_d}{x_s} < \frac{|V_{td}|^2}{|V_{ts}|^2} \leq 0.210 \quad , \tag{4.4}$$

with 90% confidence. This result will be discussed again in Chapter 7.

4.4 Parameterisation of $B^0 - \bar{B}^0$ mixing

The amount of mixing seen in the neutral B system can be described by a number of different parameters. The choice of the describing parameter usually depends on the type of work involved, i.e theory or experiment, and the contents of the sample. As can be seen in the previous section the theorists usually quote mixing in terms of x_q. Experimentalists tend to choose different parameters.

Currently $B^0 - \bar{B}^0$ mixing is measured in colliding beam experiments, where it is assessed by counting the number of B^0's that mix. This is usually done by looking at events in which a $b\bar{b}$ quark pair is created and both quarks decay semileptonically. If one quark mixes then the leptons will have the same charge, whereas if neither or both quarks mix the leptons will have opposite

signs. Therefore by counting the number of same signed pairs, and correcting for other processes that can give such a signal, e.g. having a $b \rightarrow c \rightarrow l$ decay on one side, the number of single mixed events can be measured. Experimental results are usually quoted as the ratio of the number of mixed B^0 against the number of some reference events. The choice of reference event depends on the centre-of-mass energies being used. At CLEO[18] and ARGUS[9], which operate at energies around 10.6 GeV, B^+B^- or $B_d^0\bar{B}_d^0$ pairs are created from an $\Upsilon(4S)$ decay, and the result is given with respect to the number of unmixed B_d^0's. This number can be obtained using the total number of double semileptonic decays that have opposite charges and correcting for the B^+B^- and double mixing contributions. Thus CLEO and ARGUS present their results in terms of r_d, where

$$r_d = \frac{\Gamma(B_d^0 \rightarrow \bar{B}_d^0 \rightarrow X')}{\Gamma(B_d^0 \rightarrow X)} \quad . \tag{4.5}$$

At higher energy experiments such as MAC[19], UA1[20] and experiments on LEP[21][22], there are extra problems. At these energies B_s^0's are created and they will contribute to the mixing, independent of the B_d^0's. Moreover the range of bottom hadrons produced increases enormously. Therefore it is no longer easy to determine the number of unmixed B^0 events. The reference event is now taken as any event containing bottom hadrons, and mixing is given in terms of χ, where

$$\chi = \frac{\Gamma(\bar{b} \rightarrow B^0 \rightarrow \bar{B}^0 \rightarrow X)}{\Gamma(\bar{b} \rightarrow \text{anything})} \quad . \tag{4.6}$$

This is simply the probability that a bottom quark will produce a B^0 that mixes. This probability can be split into separate contributions from B_d^0 and B_s^0 mesons. If $\mathcal{M}_q$ is the probability that a bottom quark will produce a B_q^0 meson that mixes, then

$$\chi = \mathcal{M}_d + \mathcal{M}_s \quad . \tag{4.7}$$

If χ_q is defined as the probability that a B_q^0 meson mixes and f_q is defined as the fraction of that meson in the sample, then

$$\mathcal{M}_q = f_q \cdot \chi_q \tag{4.8}$$

and

$$\chi = f_d \cdot \chi_d + f_s \cdot \chi_s \ .$$

Therefore, for a given f_d and f_s, χ will represent a straight line on the $\chi_d - \chi_s$ plane. Using this line, along with other results, it is then possible to deduce some of the properties of the top quark's contribution in the CKM matrix.

All the parameters that have been discussed are obviously related. For instance, considering a sample of B_d^0's, then integration of Equations 4.2 and 4.3 from $t = 0$ to $t \rightarrow \infty$ gives

$$r_d = \frac{x_d^2 + y_d^2}{2 + x_d^2 - y_d^2} \ , \tag{4.9}$$

where $y = \Delta\Gamma/(2 \cdot \Gamma)$ and $\Delta\Gamma = \Gamma_1 - \Gamma_2$. In $K^0 - \bar{K}^0$ mixing the $K_2 \rightarrow 3\pi$ decay is heavily suppressed due to phase space so $\Delta\Gamma \simeq \Gamma_1$ and $y \simeq 1$. In the B_2 case there no such phase space suppression and it is found that $\Gamma_1 \simeq \Gamma_2$ making $y \simeq 0$. Therefore equation 4.9 implies

$$r_d \simeq \frac{x_d^2}{2 + x_d^2} \ .$$

The relationship between χ_d and r_d is straightforward. A little algebra gives

$$\chi_d = \frac{r_d}{1 + r_d} \simeq \frac{x_d^2}{2(1 + x_d^2)} \ .$$

A similar expression can be derived for B_s^0's.

4.5 CP violation in $B^0 - \bar{B}^0$ mixing

The preceeding formalism has been discussed using the assumption that the weak force is CP invariant. However in 1964 it was shown that the $K^0\bar{K}^0$ system violates CP[23] at a very small level. This violation can be included into the $B^0\bar{B}^0$ system by redefining the decay states B_1 and B_2 to be

$$\begin{aligned} |B_1\rangle &= \frac{1}{\sqrt{2(1 + |\epsilon|^2)}}((1 + \epsilon)|B^0\rangle + (1 - \epsilon)|\bar{B}^0\rangle) \\ |B_2\rangle &= \frac{1}{\sqrt{2(1 + |\epsilon|^2)}}((1 + \epsilon)|B^0\rangle - (1 - \epsilon)|\bar{B}^0\rangle) \ , \end{aligned}$$

where ϵ is a complex number that specifies the amount of CP violation.

By repeating the derivation of r_d in equation 4.9 and also deriving $\bar{r_d}$, which is defined by a similar equation to that of 4.5 but using $\bar{B}^0$s, it is found that:

$$\begin{aligned} r_d &= \left|\frac{1-\epsilon}{1+\epsilon}\right|^2 \frac{x_d^2+y_d^2}{2+x_d^2-y_d^2} \\ \bar{r_d} &= \left|\frac{1+\epsilon}{1-\epsilon}\right|^2 \frac{x_d^2+y_d^2}{2+x_d^2-y_d^2} \end{aligned} .$$

In theory, it should be possible to measure the CP violation by studying $B^0 - \bar{B}^0$ mixing. However, $|\epsilon| = (2.26 \pm 0.02) \times 10^{-3}$[24], so CP violation is small. B^0 production at LEP is not copious enough nor clean enough to be sensitive to this small effect, so the approximation of CP invariance is used.

Chapter 5

Determining quark charges in $Z^0 \rightarrow q\bar{q}$ decays

No free quarks have even been seen from Z^0 decays. The fact that no free quarks have ever been observed at any energy is one of the basic tenets of QCD and the principle of colour confinement. However in many cases, such as in $B^0 - \bar{B}^0$ mixing and charge asymmetry, one would like to be able to extract information about the initial quarks. At the moment the process that leads from the Z^0 to the observed hadrons is not fully understood. While QCD does give an explanation as to why no free quarks are seen, it can not be solved analytically to show how the Z^0 turns into hadrons. At the moment one has to rely on fragmentation Monte Carlos to model this process.

5.1 QCD and colour confinement

QCD is derived by enforcing SU(3) symmetry on gauge fields. The 'charge' of this interaction is colour, and it is mediated by 8 different types of gluons. An important feature that comes out of the SU(3) symmetry is that the gluon fields are non-abelian, i.e. the gluon operators do not commute with each other. This leads to the fact that gluons can couple to each other and this, in turn, causes the QCD coupling constant, α_s, to increase as the momentum transfer decreases. The practical result of this behaviour is that the force between two strongly

interaction particles increases as they separate, whereas the opposite is true for electromagnetic interactions. Therefore at the energies at which particles are usually observed only neutral colour states, such as $q\bar{q}$ and qqq, can be seen. This phenomenon is known as colour confinement.

The increase in α_s, caused by the $q\bar{q}$ pair from Z^0 decay separating, means that the QCD interactions between the quarks can no longer be solved using perturbation theory. At the moment non-perturbative problems can not be solved rigorously. Instead a phenomenological approach has to be used. In this case the answer is to use a fragmentation model to simulate the transition of quarks and gluons into hadrons, and these models are implemented by means of a Monte Carlo simulation.

5.2 ALEPH's Monte Carlo

The standard Monte Carlo used by ALEPH at the time of this analysis was based on the JETSET 6.3 program[25][26]. The JETSET program has been modified to introduce a more complete simulation of the physics in ALEPH, especially for heavy flavour hadrons. This modified version is referred to as HVFL01. An enlarged decay table for both charm and bottom hadrons has been included. More importantly for this analysis $B^0 - \bar{B}^0$ mixing has been implemented, a process not included in the standard JETSET code. The mixing is done by inhibiting B^0 decays while allowing all other particles to decay normally. Then each B^0 in the event is mixed or not as dictated by the input probabilities. If the meson has been deemed to have mixed, it is then replaced by its antiparticle. Once this has been done for all B^0's in the event they are all allowed to decay as normal. The values for mixing used in the Monte Carlo production were

$$\mathcal{M}_d = 0.0642$$

and

$$\mathcal{M}_s = 0.0507 \ .$$

However, it will be seen in Chapter 6 that the new method of determining $B^0 - \bar{B}^0$ mixing used in this thesis is independent of these Monte Carlo settings.

Full $Z^0 \rightarrow q\bar{q}$ Monte Carlo production for ALEPH is done in three stages. Initially the 'generator' program, KINGAL[27], is run. This generates the $q\bar{q}$ pair using the Monte Carlo routines of DYMU 2. It then handles the fragmentation and the decay of all particles with lifetimes of less than 10^{-15} seconds using HVFLO1. The output of this program serves as the input to GALEPH[28], the full detector simulation of ALEPH built using the GEANT[29] package. In this program the particles are tracked through the detector, decayed when appropriate and any interactions with the detector are also modeled. The readout of the detector is also simulated so that the output of the program is the same as that from the real detector but with extra information about the Monte Carlo particles used to generate it. This extra information is referred to as the Monte Carlo truth. The output from GALEPH is passed onto the ALEPH reconstruction program, JULIA, which creates a fully simulated data set. This final output is known as fully reconstructed Monte Carlo.

Another, quicker, method of generating the Monte Carlo output is used to assess the effects of changes in the Monte Carlo parameters (see Subsection 6.4.1). It would be impractical to generate fully reconstructed events for each variation of a parameter. Therefore the files are generated by just running the KINGAL program but changing the maximum decay time from 10^{-15} to 10^{-8} seconds. By comparing the differences in this output with one generated the same way but using the standard Monte Carlo settings it is possible to estimate the effects of any parameter change.

5.3 Fragmentation in JETSET

The hadronisation of quarks produced in Z^0 decays is modeled by fragmentation schemes. In JETSET there are a number of possible models to choose from. The one used by ALEPH has two steps. The first step is to use the method of parton

showers to model the evolution of the quark–gluon system. The second step is to use the LUND string model to 'dress' the final quarks and gluons of the parton shower into hadrons.

5.3.1 Parton showers

The parton shower model is based on the principle that a quark can radiate a gluon, and that a gluon can either radiate another gluon or convert into a quark–antiquark pair. This branching can be iterated to give a shower of quarks and gluons. The probability that a branching will occur, creating two new particles with fractions z and $1-z$ of the parent's energy, is given by the Altarelli-Parisi equations[30]. The branching for any given quark or gluon is halted when its mass is less than $M_{\rm min}$. The standard ALEPH Monte Carlo has been tuned such that

$$M_{\rm min} = 1.5 \text{ GeV}/c^2 \ .$$

Once all quarks and gluons have dropped below $M_{\rm min}$ the resulting states are passed onto the string fragmentation part of the program.

5.3.2 LUND string model

The ideas of the LUND string model[31] can be demonstrated by considering the simplest case, that of a $q\bar{q}$ pair which is separating. A schematic of this case is shown in Figure 5.1. The two quarks are connected by a one dimensional string that represents the colour field between them. This string has a constant energy density of approximately 1 GeV^2/fm. As the quarks continue to separate, energy is transferred into the string which can then break by promoting another quark–antiquark pair ($q'\bar{q}'$) out of the vacuum. The q and $\bar{q}'$ now form the two ends of a new string segment as do the $\bar{q}$ and q'. One of these string segments is forced to become a hadron that is on its mass shell. The remaining segment can continue to fragment, thus giving the method an iterative structure. The fragmentation stops when the invariant mass of the remaining string falls below

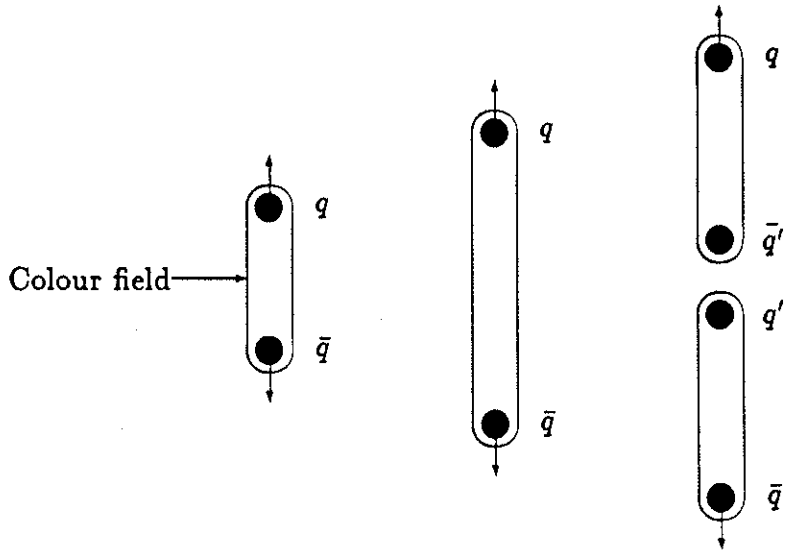

Figure 5.1: *Schematic showing the basic idea behind string fragmentation. The $q'\bar{q}'$ pair are created from energy stored in the colour field.*

a selected value. A gluon can be included in the system by introducing a kink in the colour string between the quarks. To allow for baryon creation as well as meson creation there is a probability that a diquark–antidiquark quadruplet ($q'q''\bar{q}'\bar{q}''$) will be promoted out of the vacuum rather than a quark–antiquark pair. The relative probability for $qq : q$ in the ALEPH Monte Carlo is 1:10.

The momentum of the generated hadrons, which will be important when considering momentum weighted hemisphere charge, is assigned by using a fragmentation formula $f(z)$, where z is the fraction of the string's energy taken by the hadron. For hadrons containing only light quarks the function[32]

$$f(z) \sim \frac{(1-z)^a}{z} \exp(\frac{-bm_T^2}{z})$$

is used, where a and b are parameters tuned to the data, and m_T is the string's transverse mass. The a and b parameters have been tuned on the ALEPH data to be

$$a = 0.5$$

and

$$b = 0.84 \ ,$$

For hadron that contain the heavier charm and bottom quarks the Peterson formula[33],

$$f(z) \sim \frac{1}{z(1 - 1/z - \epsilon_q/(1-z))^2} \ ,$$

where ϵ_q is a free parameter expected to scale with flavour like $\epsilon_q \propto 1/m_q^2$. During the ALEPH Monte Carlo production the values of these parameters were set to those measured in [34], namely

$$\epsilon_c = 0.020$$

and

$$\epsilon_b = 0.006 \ .$$

At the moment there is no evidence to show that these two functions do not model quark fragmentation well and that an alternative choice of $f(z)$ would be preferable.

5.4 Momentum weighted hemisphere charge

The fragmentation process leads to the initial quarks being hidden in the shower of generated hadrons making it impossible to state reliably which hadrons contain the initial quarks. Moreover heavy quarks will tend to decay before their hadrons can be observed. Therefore it is not straightforward to find out the charge of a quark that generates a jet of observable hadrons.

In 1978 Field and Feynman[35] put forward a method for determining, at least statistically, the charge of a quark that generates such a jet. The idea is based on the premise that one of the leading particles near the centre of the jet is most likely to contain the parent quark. Therefore, by taking a weighted sum of the charges of all charged particles in a jet, it should be possible to find out some information about the original quark's charge.

In this analysis the quarks' jets are defined by separating the event into two hemispheres. These hemispheres are defined by a plane though the interaction point that is perpendicular to the thrust axis. The weighting factor is chosen to be the particle's momentum parallel to the thrust axis which is raised to a selected power. The sum is normalised by the sum of the weighting factors. Thus the momentum weighted hemisphere charge (referred to from now on as the hemisphere charge), $Q_{\rm H}$, is defined by

$$Q_{\rm H} = \frac{\sum_i q_i \cdot |\mathbf{p}_i \cdot \hat{\mathbf{e}}_{\rm H}|^\kappa}{\sum_i |\mathbf{p}_i \cdot \hat{\mathbf{e}}_{\rm H}|^\kappa} \quad , \tag{5.1}$$

where q_i is the charge of particle i, $\mathbf{p}_i$ is the particle's momentum vector, $\hat{\mathbf{e}}_{\rm H}$ is the unit vector along the thrust axis in that hemisphere, κ is the selected power and i runs over all charged particles whose momentum satisfies

$$\mathbf{p}_i \cdot \hat{\mathbf{e}}_{\rm H} > 0 \quad .$$

A number of alternative weighting methods, such as rapidity, have been used by other experiments[36][37][38][39]. These choices have been found to have similar efficiencies in assigning the quarks charge to the method used in this analysis. However the momentum weighting method shows a greater sensitivity to $B^0 - \bar{B}^0$ mixing[40].

To get some idea how good $Q_{\rm H}$ is at predicting the sign of a hemisphere's parent quark the quark–signed hemisphere charge, $Q_{q\rm H}$, is constructed by

$$Q_{q\rm H} = \text{sign of quark charge} \times Q_{\rm H} \text{ of its hemisphere.} \tag{5.2}$$

The distribution of this quantity generated from 127 thousand $Z^0 \rightarrow q\bar{q}$ Monte Carlo events is shown in Figure 5.2. In the following chapters the important quantity of distributions of $Q_{q\rm H}$ will be their shape. Therefore the distribution is divided by its area to give a probability density function, $\mathcal{Q}(Q_{q\rm H})$. To make sure that the events are well contained within the detector and that they have a reasonable distribution of tracks, they are required to have $|\cos(\theta_{\rm thrust})| < 0.85$ and must contain at least two jets (for the jet definition see Subsection 6.1.2). The mean of the distribution in Figure 5.2 is $+0.1377 \pm 0.0008$ which implies

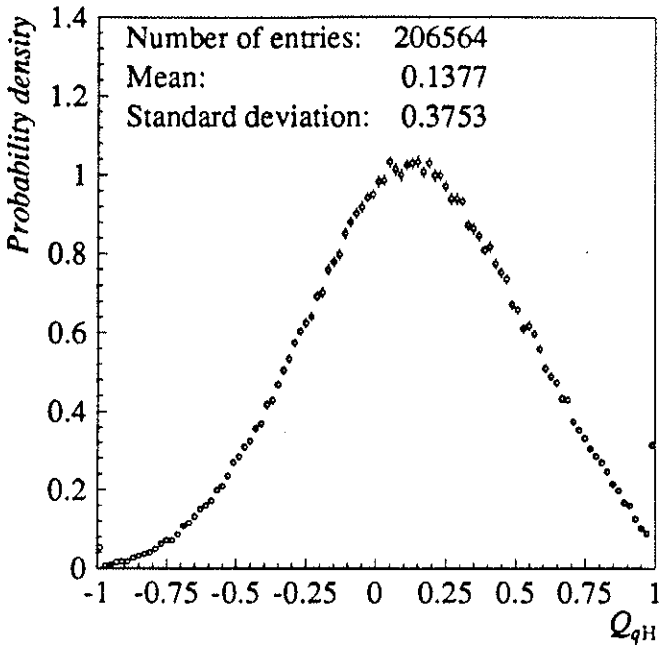

Figure 5.2: Q_{qH} *for 127 thousand* $Z^0 \rightarrow q\bar{q}$ *Monte Carlo events using* $\kappa = 1.0$. *The distribution has been divided by its area to create a probability density distribution.*

that Q_H has some power to resolve the sign of the quark's charge. However it can also be seen that there is a substantial number of Q_{qH}'s which are less than zero, indicating that the measured Q_H had the wrong sign. The effect of these charges will be to dilute the final result.

To measure how effective Q_H is at flagging the sign of the quark's charge the charge separation asymmetry, $\mathcal{A}_{sep}$, is defined as

$$\mathcal{A}_{sep} = \frac{(\text{Number of } Q_{qH} \geq 0) - (\text{Number of } Q_{qH} < 0)}{\text{Total number of } Q_{qH}} .$$

Figure 5.3 shows how this quantity varies with respect to κ, the weighting power, for each quark flavour. It can be seen for most quark flavours that $\mathcal{A}_{sep}$ is fairly constant with a slight maximum around $\kappa = 0.4$. The exception to this is the charm quark. The behaviour of the charm quark can be explained by the fact that its decays often produce a soft pion that carries the charm quark's charge information. However as this pion is soft it will not have a large contribution to Q_H due to the momentum weighting and thus the charge information is lost.

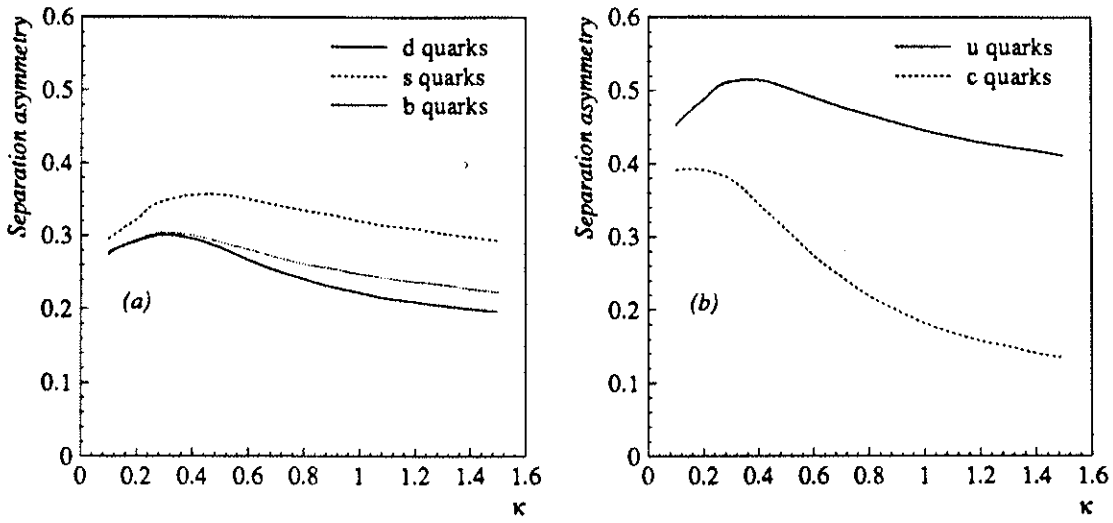

Figure 5.3: *Separation asymmetry, $\mathcal{A}_{\rm sep}$, measured from fully reconstructed Monte Carlo, for (a) charge $\frac{1}{3}$ quarks and (b) charge $\frac{2}{3}$ quarks.*

5.5 Comparing data and Monte Carlo

As the details about $Q_{q\rm H}$, such as its efficiency and shape, have to be derived from the Monte Carlo it is important to assess how well the Monte Carlo models the data. The comparison between the 1990 data and Monte Carlo is shown in Figure 5.4 using $\kappa = 1.0$. To evaluate the difference between the two distributions the χ^2 is calculated. The χ^2 is defined by

$$\chi^2 = \sum_i \frac{(\mathcal{H}_{i\ \rm Data} - \mathcal{H}_{i\ \rm MC})^2}{\sigma^2_{i\ \rm Data} + \sigma^2_{i\ \rm MC}} \quad ,$$

where $\mathcal{H}_i$ is the probability of bin i, σ_i is the error in that probability and the sum runs over all bins between -1.0 and 1.0. The χ^2 per degree of freedom between the data and Monte Carlo distributions of $Q_{\rm H}$ are shown in Figure 5.5 for the range of $0.0 < \kappa < 1.6$. At this point it should be remembered that the Monte Carlo was generated with fixed values for $\mathcal{M}_d$ and $\mathcal{M}_s$ which are not necessarily the values seen in nature, and as will be shown in Section 5.7 the amount of $B^0 - \bar{B}^0$ mixing will affect the overall hemisphere charge distribution to a small extent. Therefore full agreement between data and Monte Carlo need not be expected.

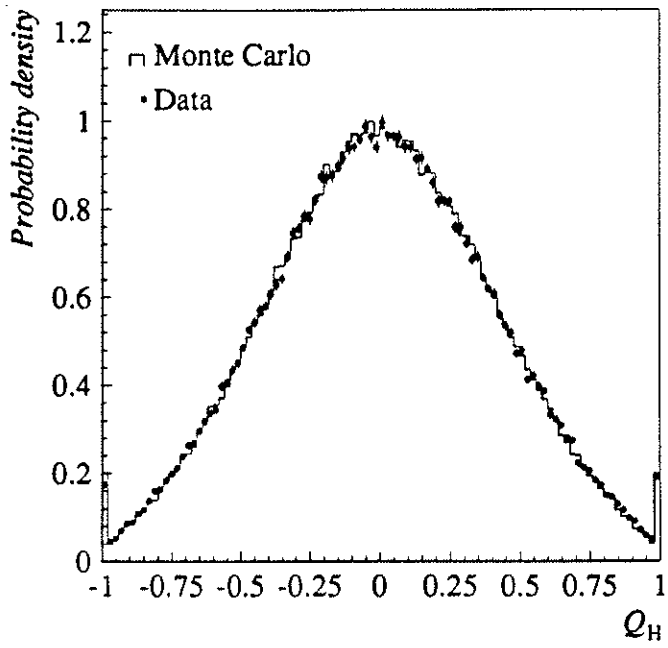

Figure 5.4: *Comparison of Q_H for 1990 data and Monte Carlo, using $\kappa = 1.0$.*

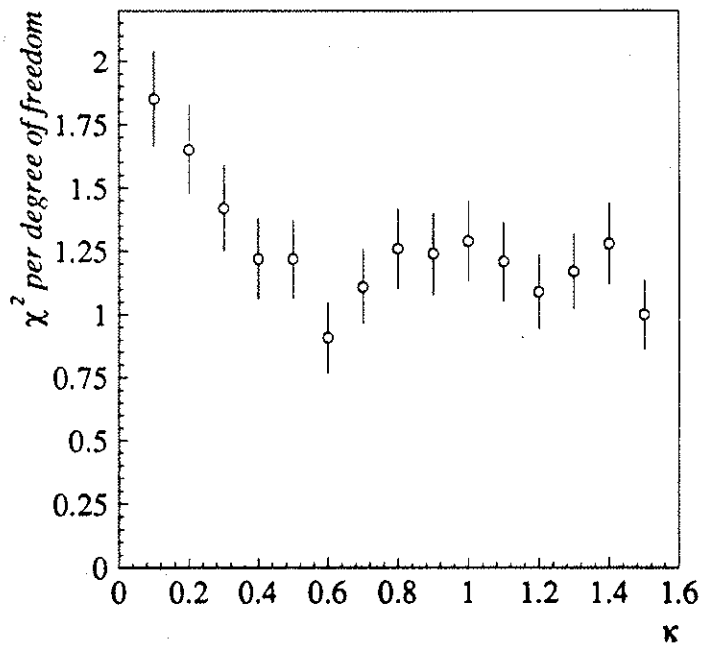

Figure 5.5: *χ^2 per degree of freedom between the 1990 data and Monte Carlo distributions of Q_H.*

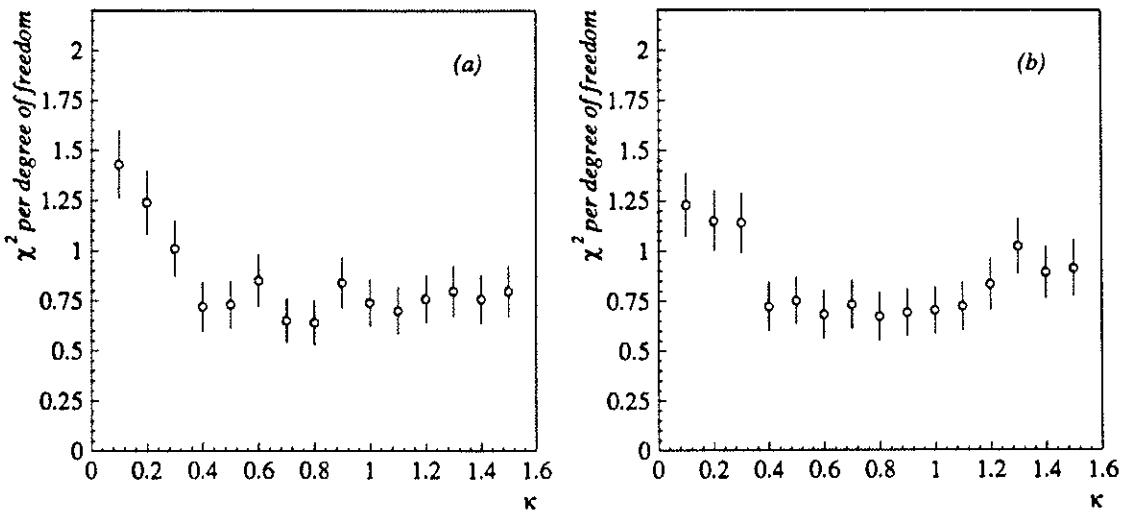

Figure 5.6: χ^2 *per degree of freedom between the 1990 data and Monte Carlo distributions of (a)* Q_+ *and (b)* Q_-.

The values for $\kappa > 0.3$ show a general consistency between data and Monte Carlo, whereas for $\kappa \leq 0.3$ there appears to be some deviation. This result is not too surprising as at low κ values low momentum tracks caused by interactions with the detector have a large effect and these are not easy to model accurately.

The Monte Carlo can also be tested against the distributions of Q_+ and Q_- which are defined by

$$Q_+ = Q_{H_1} + Q_{H_2}$$

and

$$Q_- = Q_{H_1} - Q_{H_2}$$

for each event, where Q_{H_i} is the hemisphere charge of hemisphere i. The two hemispheres are assigned their labels on an arbitrary basis to ensure an equal population of positive and negative quarks in both hemispheres 1 and 2. The χ^2 per degree of freedom between the 1990 data and Monte Carlo for the Q_+ and Q_- distributions are shown in Figure 5.6. Again the very low values of κ begin to show a deviation, while the other values show good agreement. Therefore it would appear to be better to use values of $\kappa \geq 0.4$. The effects of $\mathcal{M}_d$ and $\mathcal{M}_s$

on this distribution are small.

5.6 Independence of Q_{H_1} and Q_{H_2}

The method used in this thesis is based on the premise that the hemisphere charge is purely a function of the parent quark of that hemisphere. Implicit in this is the assumption that the distribution of Q_{qH} is independent of the value of Q_H measured in the opposite hemisphere. The main physics reasoning behind this is that as the decay of any particle is independent of the rest of the event then the only 'cross-talk' between the two hemispheres will stem from the fragmentation process. The fragmentation process handles each string segment as an independent unit up until the last segment where the energy and momentum of the event have to be conserved. This means that most particles are not correlated to the other particles in the event. However string fragmentation is only a phenomenological model and in the real world the particles may have different correlations. Therefore it is necessary to determine how true the assumption of independence is for the data. As the Q_{qH} distribution can not be measured for the data it is impossible to prove that the assumption is completely true. However it is possible to check whether the data is consistent with it by testing to see if the Q_H measured for one hemisphere is independent of the Q_H measured for the opposite one. To do this the Q_H's are divided up into separate sets, S_j, where $j = 1$ to N and N is the number of sets. The set S_j will contain all Q_H's that satisfy

$$Q_j \leq |Q_H| < Q_{j+1} \quad .$$

This is shown schematically in Figure 5.7. The values of Q_j are chosen so that each set has similar sized populations. The absolute value of Q_H is necessary in the definition of S_j so that each set has an equal contribution from positive and negative quarks. For each set the distributions of Q_H for the hemisphere opposite the set member can be histogrammed. The histograms from two different sets, j

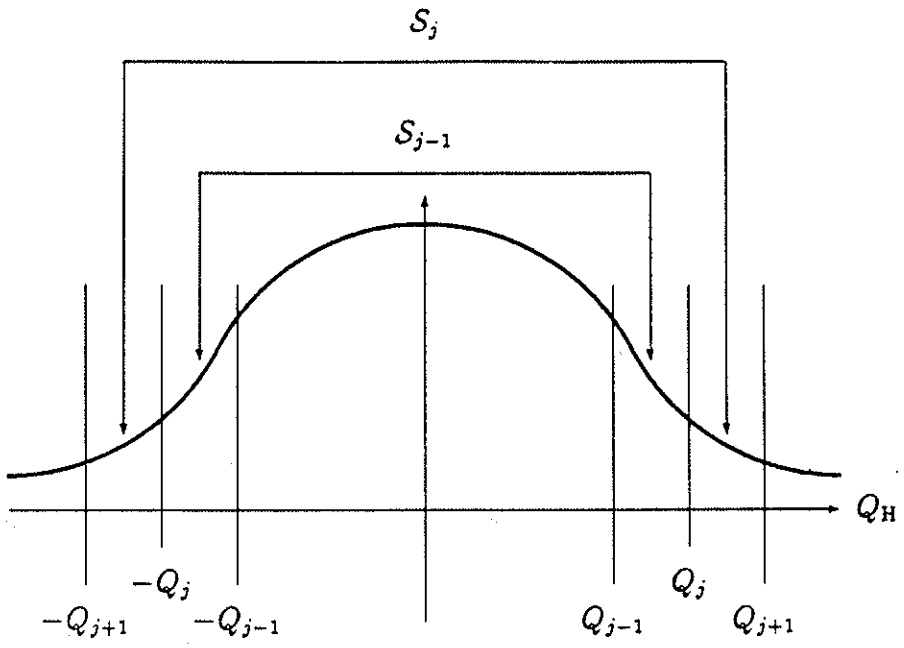

Figure 5.7: *Schematic showing how the Q_H's are divided into sets.*

and k, can then be compared by evaluating the χ^2 where

$$\chi^2 = \sum_i \frac{(\mathcal{H}_i(S_j) - \mathcal{H}_i(S_k))^2}{\sigma_i(S_j)^2 + \sigma_i(S_k)^2} \quad ,$$

where $\mathcal{H}_i(S)$ is the probability of bin i in the histogram from the set S, $\sigma_i(S)$ is the error in that probability and the sum runs over all bins between -1.0 and 1.0. The results when the sample is split into five sets and using κ values of 0.5 and 1.0 are shown in Table 5.1. The values of Q_j used to generate this table are shown in Table 5.2. The results in Table 5.1 imply that there is some dependence between Q_{H_1} and Q_{H_2} at $\kappa = 0.5$, whereas at $\kappa = 1.0$ there is no obvious sign of this dependence. To get a better idea how the dependence varies with κ Table 5.3 shows for various values of κ the χ^2 per degrees of freedom between S_1 and S_5 and the average and standard deviation of the χ^2 per degree of freedom for all ten possible combinations of j and k. It can be seen that for $\kappa \leq 0.8$ the two hemispheres have an increasing correlation as κ decreases. For

		k			
		5	4	3	2
j	1	1.90	1.34	0.80	0.89
	2	1.90	1.17	0.72	
	3	1.43	1.02		
	4	1.17			

(a) $\kappa = 0.5$

		k			
		5	4	3	2
j	1	1.17	0.90	1.08	1.11
	2	1.08	0.88	1.01	
	3	1.18	1.01		
	4	1.05			

(b) $\kappa = 1.0$

Table 5.1: χ^2 *per degree of freedom between the distributions of* Q_{H} *for hemispheres opposite members of sets* S_j *and* S_k *for* $\kappa = 0.5$ *and* 1.0.

j	Q_j	
	$\kappa = 0.5$	$\kappa = 1.0$
1	0.00	0.00
2	0.06	0.11
3	0.12	0.22
4	0.19	0.35
5	0.32	0.52
6	1.01	1.01

Table 5.2: *Values of* Q_j *used when creating Table 5.1.*

κ	χ^2 per degree of freedom		
	between $\mathcal{S}_1$ and $\mathcal{S}_5$	Average	Standard deviation
0.3	3.84	1.99	1.12
0.4	2.36	1.34	0.54
0.5	1.90	1.23	0.40
0.6	1.63	1.17	0.24
0.7	1.76	1.26	0.22
0.8	1.41	1.04	0.19
0.9	1.16	1.07	0.14
1.0	1.17	1.05	0.10
1.1	1.29	1.07	0.11

Table 5.3: *χ^2 per degree of freedom between the distributions of $Q_{\rm H}$ for hemisphere opposite members of sets $\mathcal{S}_1$ and $\mathcal{S}_5$, along with the average and standard deviation of the χ^2 per degree of freedom for all ten possible combinations for sets.*

$\kappa > 0.8$ there is still some slight correlation. This residual correlation can be explained by considering the flavour composition of each set. This composition will vary between sets as the distribution of $Q_{\rm H}$ is not identical for each flavour. However as the χ^2 per degree of freedom is close to unity the differences in the distributions can be taken to be small. Therefore the hemispheres can be considered independent for values of $\kappa \geq 0.8$.

5.7 Effects of $B^0 - \bar{B}^0$ mixing on $Q_{\rm H}$

In Chapter 6 the probability density function of $Q_{q\rm H}$ for bottom quarks, $\mathcal{Q}_b(Q_{q\rm H})$, will be used to measure $B^0 - \bar{B}^0$ mixing. Therefore it is important to understand if and how $B^0 - \bar{B}^0$ mixing will affect $\mathcal{Q}_b$. The function $\mathcal{Q}_b$ can be considered to

be the combination of five separate distributions, namely:

$\mathcal{Q}_{\rm NB}$: $\mathcal{Q}_b$ of hemispheres not containing a B^0.

$\mathcal{Q}_{\rm DU}$: $\mathcal{Q}_b$ of hemispheres containing a B_d^0 that has not mixed.

$\mathcal{Q}_{\rm DM}$: $\mathcal{Q}_b$ of hemispheres containing a B_d^0 that has mixed.

$\mathcal{Q}_{\rm SU}$: $\mathcal{Q}_b$ of hemispheres containing a B_s^0 that has not mixed.

$\mathcal{Q}_{\rm SM}$: $\mathcal{Q}_b$ of hemispheres containing a B_s^0 that has mixed.

Therefore $\mathcal{Q}_b$, in terms of these distributions, is

$$\begin{aligned}\mathcal{Q}_b &= (1-f_d-f_s)\cdot\mathcal{Q}_{\rm NB} + f_d\cdot(1-\chi_d)\cdot\mathcal{Q}_{\rm DU} + f_d\cdot\chi_d\cdot\mathcal{Q}_{\rm DM} \\ &\quad + f_s\cdot(1-\chi_s)\cdot\mathcal{Q}_{\rm SU} + f_s\cdot\chi_s\cdot\mathcal{Q}_{\rm SM} \ . \end{aligned} \tag{5.3}$$

The separation asymmetries for these five distributions are shown in Figures 5.8 and 5.9. It can be seen from Figure 5.9 that mixing has a significant effect on $\mathcal{A}_{\rm sep}$ and thus on the hemisphere charge. The difference between the $\mathcal{A}_{\rm sep}$ for hemispheres containing unmixed B^0's and those containing mixed B^0's can be explained by considering the contributions to the hemisphere charge of the descendants of a B^0 and from the fragmentation products separately. Figure 5.10 shows how a $\bar{b}$ quark together with a quark, q, pulled from the vacuum form a B_q^0 meson and leave a $\bar{q}$ quark to continue fragmentation. If $Q_{B_q^0}$ is defined by equation 5.1 but with the summation in the numerator being restricted to the descendants of the B_q^0, and if Q_q is similarly defined but with the summation restricted to all particles that are not descendants of the B_q^0, then

$$Q_{\rm H} = Q_{B_q^0} + Q_q \ .$$

Charge conjugation implies

$$Q_{B_q^0} = -Q_{\bar{B}_q^0} \ ,$$

so if the B_q^0 mixes into a $\bar{B}_q^0$ then the hemisphere charge becomes

$$Q_{\rm H} = -Q_{B_q^0} + Q_q \ .$$

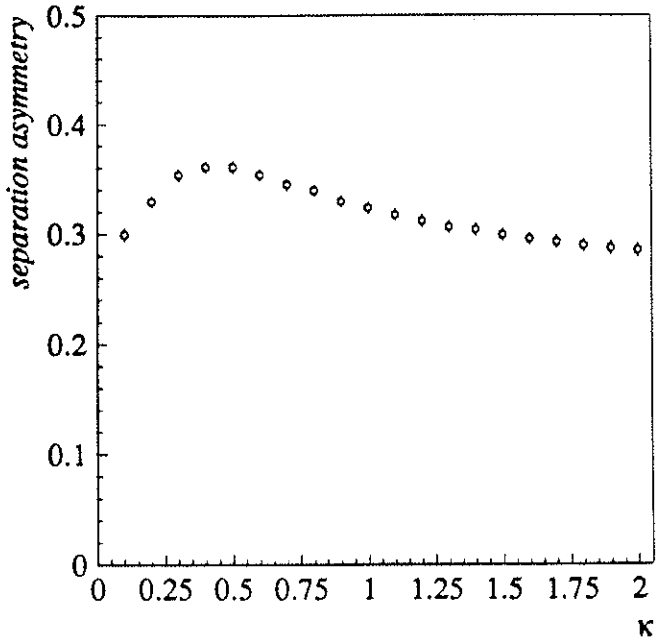

Figure 5.8: *Separation asymmetry, $\mathcal{A}_{\rm sep}$, derived from the Monte Carlo, for hemispheres in bottom quark events that do not contain a B^0.*

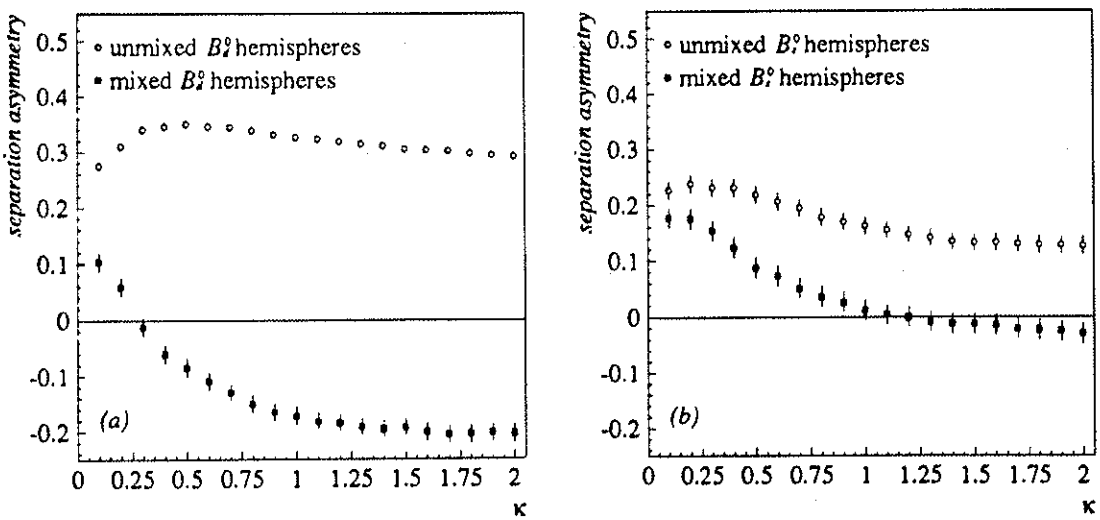

Figure 5.9: *Separation asymmetry, $\mathcal{A}_{\rm sep}$, derived from the Monte Carlo, for hemispheres containing (a) unmixed and mixed B_d^0's, and (b) unmixed and mixed B_s^0's.*

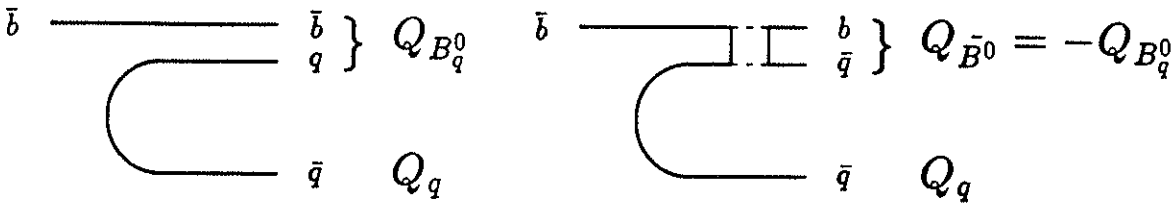

Figure 5.10: *Schematic showing how the hemisphere charge for B^0 events can be broken down into a part from the descendant of the B^0, $Q_{B_q^0}$, and a part from the fragmentation products, Q_q. The effect of $B^0 - \bar{B}^0$ mixing is shown on the right.*

It is apparent that if $Q_{B_q^0}$ is non-zero then hemispheres containing unmixed B^0's and those which contain mixed B^0's will have different distributions of $Q_{q\mathrm{H}}$. This can lead to different values for $\mathcal{A}_{\mathrm{sep}}$. Figure 5.9 shows that this is indeed observed. By comparing the results in this figure it can be seen that on average $Q_{B_d^0} > Q_d$, while $Q_{B_s^0} \approx Q_s$ for $\kappa \geq 1.0$. As both $Q_{B_d^0}$ and $Q_{B_s^0}$ are non-zero then when Q_b is used to measure $B^0 - \bar{B}^0$ mixing it must contain terms reflecting the changes with mixing.

Chapter 6

$B^0 - \bar{B}^0$ mixing using lepton–signed hemisphere charges

$B^0 - \bar{B}^0$ mixing at the Z^0 pole is usually quantified by the mixing parameter χ, defined by equation 4.6. Therefore any measurement of mixing should ideally only use $Z^0 \rightarrow b\bar{b}$ events. However ALEPH records many different types of physics events: $Z^0 \rightarrow q\bar{q}$ (hadronic), $Z^0 \rightarrow l\bar{l}$ (leptonic), two photon, beam–gas interactions and cosmic ray events. To make a good measurement of $B^0 - \bar{B}^0$ mixing as many background, i.e. non-$b\bar{b}$, events as possible should be removed, thus creating a $b\bar{b}$ enriched sample.

6.1 Selecting a $Z^0 \rightarrow b\bar{b}$ enriched data sample

The enriched $b\bar{b}$ sample is created in two stages. As hadronic events can be readily separated from the other types of events, a hadronic sample is created first. Then this sample is passed through some algorithm that is more likely to choose $b\bar{b}$ events than the other $q\bar{q}$ events.

6.1.1 Selection of hadronic events

A hadronic event can be distinguished from the other types by its charged track characteristics. First a good charged track is defined by:

- four or more TPC coordinates are associated with the track;

- $|\cos(\theta)|$ of the track is less than 0.95;
- its closest approach to the beam axis in the $r - \phi$ plane (known as the track's d_0) is less than 2.0 cm;
- its z coordinate at the point of closest approach to the beam axis (known as the track's z_0) is less than 10.0 cm.

The first two criteria ensure that the track is well reconstructed. The final pair remove tracks from beam gas interactions and cosmic ray events. Then, by considering all good tracks, an event is classed as hadronic if it has both of the following:

- five or more good charged tracks;
- the total energy of the charged tracks is greater the 10% of the centre-of-mass energy.

The multiplicity requirement removes most of the leptonic events, except six and greater prong $\tau^+\tau^-$ events. The energy criteria rejects most two photon events.

This method of hadronic selection has been shown to have a $(97.3 \pm 0.3)\%$ efficiency in ALEPH[41], and the major background is $\tau^+\tau^-$ events which are at the level of $(0.26 \pm 0.03)\%$.

6.1.2 Tagging $b\bar{b}$ quark events with high $p_\perp$ leptons

The $b\bar{b}$ decays of a Z^0 cannot be uniquely separated from other hadronic decays. All that can be done is to tag events which have a characteristic that is more likely to exist in a $b\bar{b}$ event than any other hadronic event. A number of methods have been developed for $b\bar{b}$ tagging. Most of these use the fact that the b quark is significantly more massive than the other four flavours produced by Z^0 decay. This extra mass means that the hadronic showers from decaying bottom hadrons are generally broader and have a higher multiplicity than those from lighter hadrons.

One method used by TASSO[42] was to divide each event into two halves by a plane perpendicular to the sphericity axis and then Lorentz boost each half along this axis. The amount of boost was optimised by Monte Carlo studies to maximise the separation of heavy flavour events. The sphericity of each half was calculated within its boosted frame and the two values multiplied together to create a 'sphericity product'. An event was then chosen if its sphericity product was above a selected threshold. The idea behind this method is that the bottom hadrons will have a lower boost than the other quark flavours, due to their larger mass. Therefore if the boosted frame is correctly chosen bottom hadrons will have a higher sphericity in both halves than the other flavours, which leads to a bottom event having a higher sphericity product.

Another method used[43] was to take all charge tracks in an event and find their intersections with each other in the $r-\phi$ plane. The distances between each intersection and the interaction point were then used to create a weighted sum for the whole event. Again an event was chosen if its sum was above a selected threshold. The principle behind this idea is that *uds* events tend to have all their tracks originating from the interaction point. However heavy quark events will usually have decay vertices displaced from the interaction point. This fact in conjunction with the higher average multiplicity seen in heavy flavour events will cause heavy flavour events to have higher values for their sums.

However, both these techniques rely, in some way, on the event's shape and this may bias the hemisphere charges for the selected events. Moreover neither of these methods provide any information about the bottom hadrons that are in the event.

The method used in this analysis is to tag events which contain a high $p_\perp$ lepton, where $p_\perp$ is the momentum of the lepton transverse to the axis of its associated jet. This favours heavier quarks as their decay leptons tend to have larger momenta and, as momentum perpendicular to the boost axis is independent of the frame of measurement these leptons will have a harder $p_\perp$ spectrum.

A jet is defined by a scaled invariant mass algorithm[44]. For each pair of

particles, i and j, their invariant mass is calculated by

$$M_{ij}^2 = 2E_iE_j(1 - \cos\theta_{ij}) \quad ,$$

which is then scaled to give

$$y_{ij} = \frac{M_{ij}^2}{E^2} \quad ,$$

where E is the scaling energy. The pair of tracks which have the lowest value of y_{ij} are then replaced by a pseudo–particle with momentum $(\mathbf{p}_i + \mathbf{p}_j)$. This procedure is iterated until the lowest value of y_{ij} is greater than a cutoff value $y_{\rm cut}$.

In this analysis E is fixed to 91.5 GeV and $y_{\rm cut}$ is chosen to be 0.004[45]. This means that the iterations finish at a jet mass of about 5.8 GeV, which is slightly larger than the rest mass of the b quark. The idea behind this is that the jet should then contain the majority of the b hadron's decay products, but clustering will stop before many fragmentation particles that are included in the jet.

To assess the contents of this tagged sample a binned fit is done to the $p - p_\perp$ spectrum[21]. The input to the fit is the $p - p_\perp$ spectrum, from the Monte Carlo, of the following 6 processes

- $b \rightarrow e$ or μ, known as primary b decay (bl);
- $b \rightarrow c \rightarrow e$ or μ and $b \rightarrow W \rightarrow \bar{c} \rightarrow e$ or μ, known as secondary c decay (sc);
- $b \rightarrow \tau \rightarrow e$ or μ, known as τ decay ($b\tau$);
- $c \rightarrow e$ or μ, known as primary c decay (c);
- electrons or muons from non–heavy quarks decays, e.g. photon conversions or pion decay. These are known as non–prompt (np);
- hadrons that are identified as electrons or muons. These are known as misidentified hadrons (had).

The output from the fit is a set of probabilities, $\mathcal{P}_{bl}, \mathcal{P}_{sc}, \mathcal{P}_{b\tau}, \mathcal{P}_c, \mathcal{P}_{\rm np}$, and $\mathcal{P}_{\rm had}$ respectively, which are functions of p and $p_\perp$, and gives the probabilities that

an electron or muon came from these processes. These probabilities can then be summed for the whole sample to give a final composition. These probabilities will also be used in the final determination of mixing.

6.1.3 Prompt electron identification

Electrons in ALEPH are identified by using three estimators, R_L, R_T and R_I. All three estimators give a Gaussian distribution for electrons. Therefore, for simplicity, each is normalised by

$$R_X = \frac{X - \langle X \rangle}{\sigma(X)} \quad , \tag{6.1}$$

where $\langle X \rangle$ is the mean and $\sigma(X)$ is the standard deviation of the quantity X for electrons. The values for these are derived from test beam measurements and fits to the data.

The R_T and R_L estimators for a track measure the transverse and longitudinal development of the electromagnetic shower in the ECAL that is associated with the track. The track is extrapolated through the ECAL and, for each of the three stacks in the ECAL, the 4 tower segments that are closest to the extrapolation are found. The energies in these segments are summed to give an energy, E_i, for each stack, where i is the stack number. The three stack energies are summed to give E_0, the energy deposited in the 4 towers around the track. From these quantities R_T is calculated using Equation 6.1 and the definition

$$T = \frac{E_0}{p} \quad ,$$

while R_L is calculated using the definition

$$L = \frac{E_0}{\sum_{i=1}^{3} E_i S_i} \quad ,$$

where S_i is the shower's mean longitudinal position in stack i.

R_I reflects the dE/dx measurement of the track. At least 50 isolated wire hits in the TPC are required for a track to be considered to a have a useful dE/dx measurement. R_I is then calculated using equation 6.1 and defining I as the 60% truncated mean of the dE/dx.

For a track to be considered as an electron it must first be a good track (see Subsection 6.1.1) with, in addition, $p \geq 2.0$ GeV/c and $|\cos(\theta)| < 0.92$. It must then pass the following cuts on the estimators:

$$\begin{aligned} -1.6 \leq \; & R_T \; ; \\ -1.8 \leq \; & R_L \; \leq 3.0 \; ; \\ -2.5 \leq \; & R_I \; . \end{aligned}$$

A track that is identified as an electron may not have come from a decay of a heavy quark but could be either a non-prompt lepton or a misidentified hadron. To minimise these backgrounds the track is rejected as a prompt electron candidate if it has one of the following features:

- less than 5 cells have been 'fired' in the ITC along the path of the track;
- the track's d_0 is greater than 0.5 cm.

Futhermore, as an extra test to see if the electron comes from a photon conversion, it is paired with every other track in the event which has the opposite sign. If any pairing has all of the following properties:

- the separation in the $r - \phi$ plane at their point of closest approach is less that 1.0 cm;
- the separation in the z plane at their point of closest approach is less that 1.0 cm;
- The invariant mass of the pair, calculated assuming electron masses, at their point of closest approach is less that 20 MeV/c^2;

then the track is flagged as a definite conversion.

6.1.4 Prompt muon identification

Muons in ALEPH are identified by considering the pattern of hits around a track's extrapolation into the HCAL and through the muon chambers. The

extrapolation takes into account the curvature caused by the magnetic field. A cone around the track is set up 3σ away from the extrapolated line, where σ is the standard deviation of the displacement caused by multiple scattering. A plane of streamer tubes is deemed to have been fired by the track if there are between 1 and 4 hits lying within the cone on that plane. In the case where two tracks' cones overlap a likelihood function is generated from the HCAL hits in this area and the tracks extrapolated position. The hits are associated to the track which has the highest likelihood.

To be considered as prompt muon candidate the track must first be a good track with the additional requirements that $p \geq 3.0$ GeV/c and $d_0 < 0.5$ cm. Then the track's hit pattern must have all of the following features[34][45]:

- at least nine planes are expected to be hit;
- the number of planes that have fired must be greater than 0.4 $\times$ the number of expected planes;
- at least five planes in the last possible ten have fired;
- the average hit multiplicity per plane over the last ten expected planes is less than 1.5;
- there is at least one hit in the muon chambers that is within 4σ of the track's extrapolated position.

The efficiencies of the electron and muon identifications, measured from the data, are shown in Table 6.1[45], along with the efficiencies for pions to be identified as electrons and hadrons to be identified as muons.

6.1.5 Data selection

Having decided the requirements for selecting a $b\bar{b}$ enriched sample, a subset of ALEPH data can be created. Only those runs with a PERF or MAYB quality flag were initially considered. All these runs where then checked to see that the parts

efficiency	$p_\perp$	
	0.0–1.0 GeV/c	1.0–2.5 GeV/c
ϵ_e	61.1 ±2.2	74.3 ±2.2
ϵ_π	0.082±0.016	0.034±0.012
ϵ_μ	71.7 ±2.2	73.8 ±2.2
ϵ_h	0.094±0.047	0.16 ±0.08

Table 6.1: *Efficiencies of electron and muon identification, along with the efficiencies for identifying a pion as an electron and a hadrons as a muon[45]. All tracks have* $3 \leq p \leq 23$ *GeV/c.*

of the apparatus necessary for lepton identification, i.e. the TPC, the ECAL, the HCAL and the muon chambers, were working reliably. If they were not the run was ignored. From the set of remaining runs an initial set of hadronic events was selected by requiring that each event had all detector high voltages on, that all the necessary triggers were enabled and that it passed the requirements set out in Subsection 6.1.1.

Each event in the hadronic sample was passed through the electron and muon identification routines. The 1989 data was only passed through the electron identification routines as the muon chambers were not fully operational during that period which meant that muon identification was not reliable for that data. If either at least one electron with $p > 2$ GeV/c or at least one muon with $p > 3$ GeV/c was found then the event was put into the lepton subset. At this stage no check was made to see if an electron was identified as a conversion.

Finally each event in the lepton sample had to pass the following requirements:

- $|\cos(\theta_{\text{thrust}})| < 0.85$;
- at least two jets were found in the event;
- it contained at least one high $p_\perp$ lepton.

A high $p_\perp$ lepton was defined as a lepton that was not flagged as a definite

Year	Hadron Sample	Lepton Sample	Final sample
1989	18892	1340	471
1990	154113	24266	9693
Total	173005	25606	10164

Table 6.2: *Number of events in each sample. In the 1989 data only electrons are identified. In the 1990 data both electrons and muons are identified.*

conversion, and had $p > 3.0$ GeV/c and $p_\perp > 0.5$ GeV/c. The first two requirements for the event ensures that it is well contained within the detector and that it has a reasonable distribution of tracks. The third enriches the sample in $b\bar{b}$ events as these are more likely to have a high $p_\perp$ lepton.

The results of these selections are shown in Table 6.2, while the composition of the final sample of high $p_\perp$ leptons is shown in Table 6.3. There are more leptons in Table 6.3 than final events in Table 6.2 as one event may contain more than one high $p_\perp$ lepton, in which case all high $p_\perp$ leptons were considered.

6.2 Lepton signed hemisphere charge

For a sample of pure primary b decays each lepton will have the same charge sign as the decaying b quark. If the decaying bottom hadron has not mixed then the lepton will have the opposite charge sign to that of the other b quark created by the Z^0 decay. Therefore, if the lepton-signed hemisphere charge, Q_{lH}, is defined by

$$Q_{lH} = -1 \times \text{sign of lepton charge} \times Q_H \text{ of opposite hemisphere} \ ,$$

then the probability density function (p.d.f.) of Q_{lH} for a lepton from an unmixed bottom hadron is simply $\mathcal{Q}_b(Q_{lH})$ (see Section 5.7 for the definition of $\mathcal{Q}_b$). In the case where the bottom hadron has mixed the lepton will have the same sign

Process	Electrons		Muons		All	
	Events	Fraction	Events	Fraction	Events	Fraction
primary b	2638	0.56	2841	0.45	5479	0.50
secondary c	912	0.19	1042	0.17	1954	0.18
τ decay	79	0.02	86	0.01	165	0.01
primary c	659	0.14	784	0.12	1443	0.13
Non-prompt	243	0.05	1141	0.18	1384	0.12
Hadrons	171	0.04	440	0.07	611	0.06
Total	4702		6334		11036	

Table 6.3: *Composition of the sample of high $p_\perp$ leptons. Each lepton in the sample is required to have $p \geq 3.0$ GeV/c and $p_\perp \geq 0.5$ GeV/c.*

as the other b quark so the p.d.f. for this case will be $\mathcal{Q}_b(-Q_{l\mathrm{H}})$. These two quantities can be combined to give the p.d.f. of $Q_{l\mathrm{H}}$ for all primary b leptons, ℓ_b, namely,

$$\begin{aligned} \ell_b(Q_{l\mathrm{H}}) &= (1 - \mathcal{M}_d - \mathcal{M}_s) \cdot \mathcal{Q}_b(Q_{l\mathrm{H}}, \mathcal{M}_d, \mathcal{M}_s) \\ &+ (\mathcal{M}_d + \mathcal{M}_s) \cdot \mathcal{Q}_b(-Q_{l\mathrm{H}}, \mathcal{M}_d, \mathcal{M}_s) \ . \end{aligned} \tag{6.2}$$

Here $\mathcal{Q}_b$ is the distribution of $Q_{b\mathrm{H}}$, while $\mathcal{M}_d$ and $\mathcal{M}_s$ quantify the amount of B^0_d and B^0_s mixing in the sample (see Equation 4.8). Therefore, given a pure sample of primary b leptons and using Equation 5.3 for $\mathcal{Q}_b$ it would be possible to perform a fit to the distribution of $Q_{l\mathrm{H}}$ to obtain limits on $\mathcal{M}_d$ and $\mathcal{M}_s$.

To do the fit it is necessary to know the p.d.f. of each of the five components in Equation 5.3 ($\mathcal{Q}_{\mathrm{NB}}$, $\mathcal{Q}_{\mathrm{DU}}$, $\mathcal{Q}_{\mathrm{DM}}$, $\mathcal{Q}_{\mathrm{SU}}$ and $\mathcal{Q}_{\mathrm{SM}}$). As these can not be measured from the data they have to be derived from the Monte Carlo. To create a smooth p.d.f. a double Gaussian fit is made to each distribution. Double Gaussians were used as they were found to give good representations of the distributions generated with $\kappa = 1.0$. The functions used to model the $\mathcal{Q}_b$'s for non-B^0, B^0_d

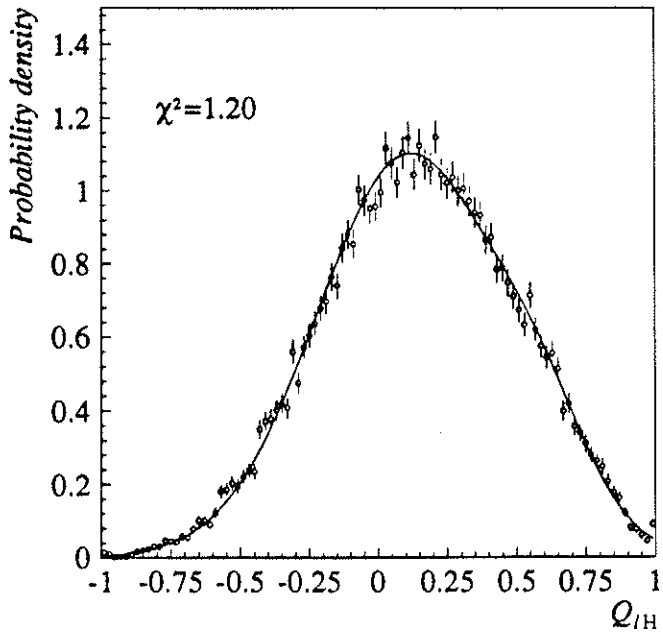

Figure 6.1: *Double Gaussian fit used to model* Q_{NB} *at* $\kappa = 1.0$.

and B_s^0 with $\kappa = 1.0$ are shown in Figures 6.1, 6.2 and 6.3 respectively.

However, as Table 6.3 shows, the subset of ALEPH data does not consist purely of primary b leptons. Therefore the background contributions must be considered when any fit to the data is done.

6.2.1 Secondary c decays

The secondary c decays can be split into two parts. The first part is where the b quark decays into a c which then decays semileptonically, while the second part is where the b decays into a $\bar{c}$ via W boson and the $\bar{c}$ then decays semileptonically. These two cases are shown schematically in Figure 6.4 If, looking at the first case,

$$\frac{\mathrm{Br}(b \rightarrow c \rightarrow l) \text{ for } B_q^0}{\mathrm{Br}(b \rightarrow c \rightarrow l) \text{ for non}-B^0} = 1 \quad , \tag{6.3}$$

is true for both B_d^0 and B_s^0, then $\mathcal{M}_d$ and $\mathcal{M}_s$ will not be affected by including these decays, providing the change in lepton's charge sign is included. The charge sign of these secondary leptons will be opposite to those coming from prompt decays of the b quarks. Therefore the p.d.f. of Q_{lH} for these decays will be the

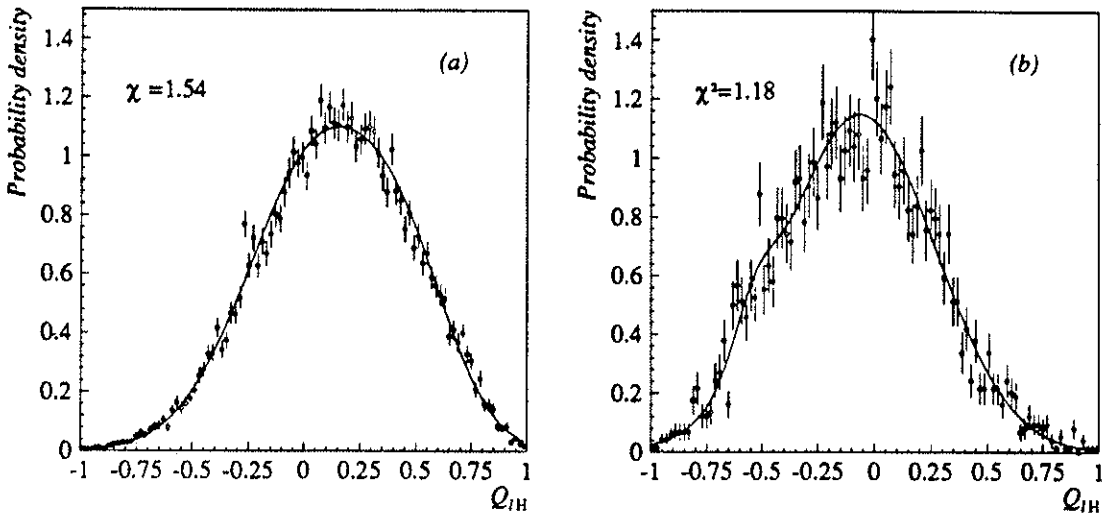

Figure 6.2: *Double Gaussian fits used to model (a)* Q_{DU} *and (b)* Q_{DM} *at* $\kappa = 1.0$.

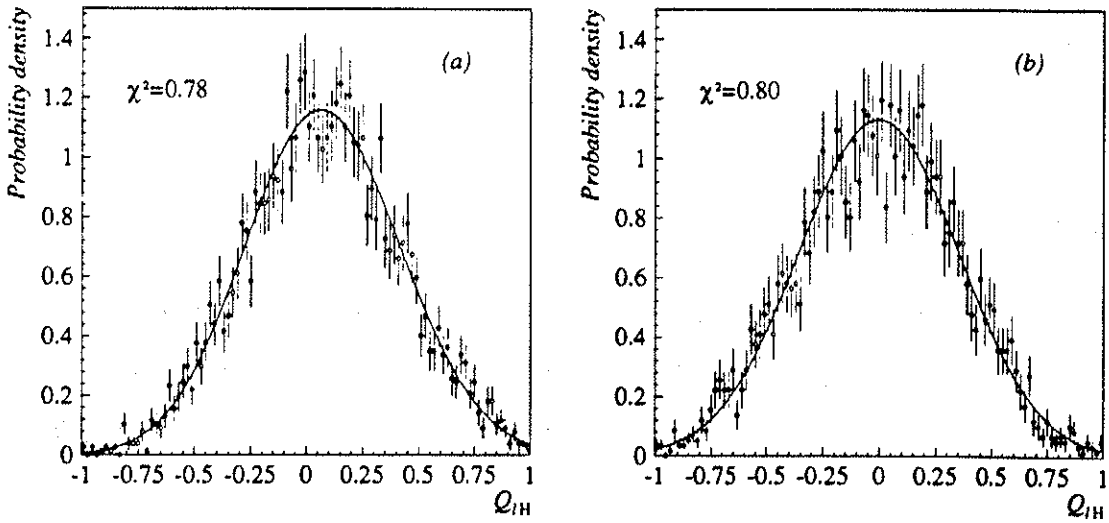

Figure 6.3: *Double Gaussian fits used to model (a)* Q_{SU} *and (b)* Q_{SM} *at* $\kappa = 1.0$.

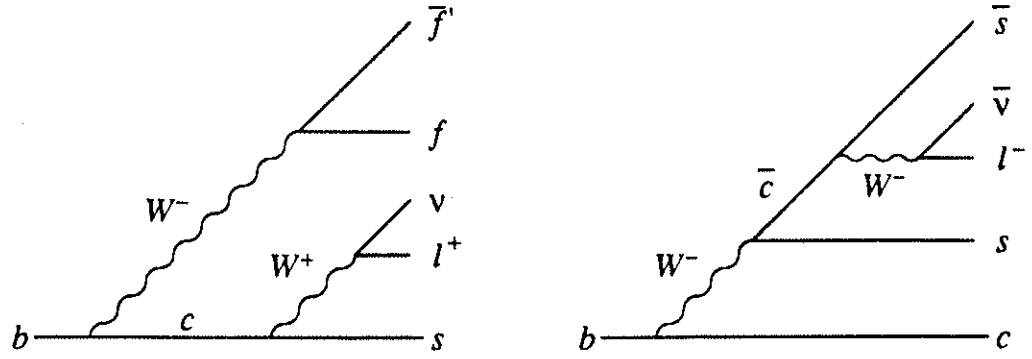

Figure 6.4: *Schematic showing the two types of secondary c decay. In the lefthand figure f can stand for an l^-, d or s and then f' will stand for a ν, u or c respectively.*

same as equation 6.2 but with Q_{lH} replaced by $-Q_{lH}$, so

$$\begin{aligned} \ell_{bc}(Q_{lH}) &= (1 - \mathcal{M}_d - \mathcal{M}_s) \cdot \mathcal{Q}_b(-Q_{lH}, \mathcal{M}_d, \mathcal{M}_s) \\ &+ (\mathcal{M}_d + \mathcal{M}_s) \cdot \mathcal{Q}_b(Q_{lH}, \mathcal{M}_d, \mathcal{M}_s) \ . \end{aligned}$$

It is assumed that a similar equation to Equation 6.3 holds true for the second case ($b \rightarrow W \rightarrow \bar{c} \rightarrow l$). For this case the secondary leptons' sign will be the same as those for primary b leptons, so

$$\ell_{bW}(Q_{lH}) = \ell_b(Q_{lH}) \ .$$

6.2.2 Primary c decays

As $D^0 - \bar{D}^0$ mixing is small (less than 0.0037[46]) it will be assumed to be zero. This means that a primary c lepton will always have the opposite sign to the c quark created in the other half of the event. Therefore the the p.d.f. of Q_{lH} for a lepton from a primary c decay is simply

$$\ell_c(Q_{lH}) = \mathcal{Q}_c(Q_{lH}) \ .$$

Again this p.d.f. can not be derived from the data and so a double Gaussian fit is done to the Q_{cH} distribution of the Monte Carlo. This fit is shown in Figure 6.5.

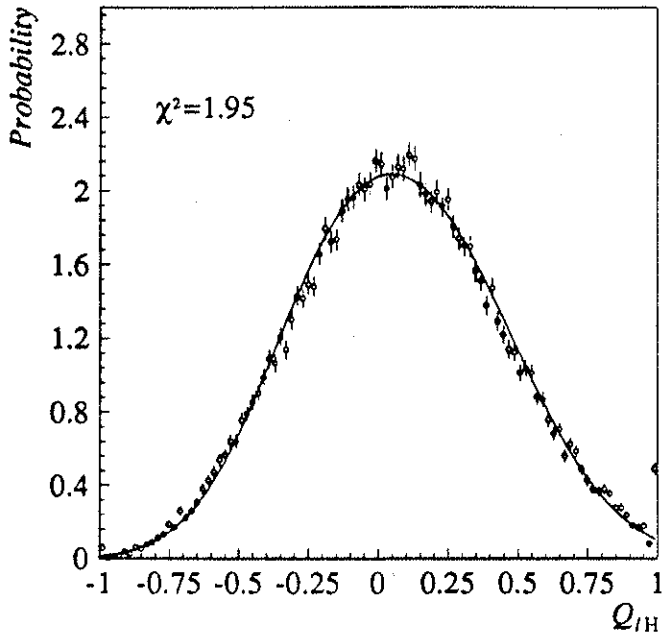

Figure 6.5: *Double Gaussian fit used to model Q_c at $\kappa = 1.0$.*

6.2.3 τ decays

For τ decays of the b quark the lepton from the τ will have the same charge sign as the decaying b quark.

If an equation similar to Equation 6.3 holds true for τ decays then these leptons will correctly reflect the mixing of the b quark and so

$$\ell_\tau(Q_{lH}) = \ell_b(Q_{lH}) \ .$$

6.2.4 Misidentified hadrons

It is assumed that the probability of misidentifying a hadron as a lepton is only a function of the track's kinematics. This assumption means the ℓ_{had} can be assessed from the data. It is possible to create a sample of 'non–leptons' which are particles that have the same kinematic properties as identified prompt leptons but are identified as not being leptons. In the case of non–electrons the track's estimators must pass at least one of the following cuts:

$$R_T \ < \ -3.0 \ ;$$

$$R_L < -1.8 \ ;$$

$$R_L > 3.0 \ .$$

For non–muons the track's extrapolation is still required to pass through at least nine planes and its hit pattern must have at least one of the following features:

- less than 0.4 of the number of expected planes that could fire have actually fired;
- less than five planes in the last possible ten have fired;
- the average hit multiplicity per plane over the last ten expected planes is greater than 2.05.

In this analysis $\ell_{\rm had}$ is modeled by a single Gaussian. To find the parameters of this Gaussian the non–leptons in the data are divided up into sets according to their p and $p_\perp$. For each set a Gaussian is fitted to the distribution of $Q_{l\rm H}$. This fit produces a mean and sigma for that set. Each set is also assigned the average values of the p and $p_\perp$ of the tracks in the set. Using these values of p and $p_\perp$ as coordinates in a 2-dimensional plane, four fits are done. These fits are done to the means and sigmas of the non–electrons and non–muons. Various functions were tried and by considering both their simplicity and their χ^2 the most appropriate functions were chosen to be:

$$\langle Q_{l\rm H} \rangle = a_1 + a_2 \cdot p \ ,$$

and

$$\sigma(Q_{l\rm H}) = b_1 + b_2 \cdot p_\perp \ ,$$

where $a_{1,2}$ and $b_{1,2}$ are numbers derived from the fits. The p dependence of the the mean is consistent with the premise that the leading tracks carry information about the parent quark (see Section 5.4). The $p_\perp$ dependence of the sigmas can be understood by considering the flavour composition of the sample. As heavier quarks have less well collimated jets they are more likely to have high $p_\perp$ hadrons. Therefore the high $p_\perp$ sample of non–leptons will have a higher proportion of

Favour	Mean of Q_{qH}	Standard deviation of Q_{qH}
up	0.22	0.37
down	0.11	0.38
strange	0.15	0.38
charm	0.07	0.38
bottom	0.12	0.35

Table 6.4: *Mean and standard deviation of Q_{qH}, derived from Monte Carlo, for each flavour using $\kappa = 1.0$.*

heavy quark events. The final sample is made up of contributions from all five flavours. The mean and standard deviation of Q_{qH} for each flavour, taken for the Monte Carlo, is shown in Table 6.4. It can be seen from these numbers that a change in composition can lead to a change in overall width of the total shape.

The fits to the data gave:

$$\langle Q_{lH} \rangle = -0.0074 + 0.0036 \times p$$

for non electrons;

$$\langle Q_{lH} \rangle = -0.0031 + 0.0028 \times p \tag{6.4}$$

for non–muons;

and

$$\sigma(Q_{lH}) = 0.416 - 0.014 \times p_{\perp} \tag{6.5}$$

for both non–electrons and non–muons.

6.2.5 Non–prompt decays

The shape of ℓ_{np} is also modeled by a Gaussian. The available statistics for definite, identified, non-prompt decays make it impossible to determine ℓ_{np} using a similar approach to that of the previous section. Instead the parameters are derived from those measured for misidentified hadrons.

Non-prompt muons are mainly due to decays of kaons and muons. For the muon to be identified in the HCAL the track must point towards the muon's HCAL digital pattern (see Subsection 6.1.4). Therefore, apart from decays that happen early in flight, the paths of the hadron and muon must be very similar. In many cases the hadron actually decays in the calorimeter so the associated track is that of the parent hadron. This means that the measured momentum of a non-prompt muon is very close to that of its parent hadron. Therefore $\ell_{\rm np}$ for muons can be reasonably modeled by using the same parameters as those measured for non-muons, i.e. Equations 6.4 and 6.5.

Non-prompt electrons are mainly due to conversions of photons, which in turn come from π^0 decays. Therefore the kinematics of the resulting electron has very little correlation with the rest of the event. This means that the parameters of $\ell_{\rm np}$ for these electrons should be independent of p and $p_\perp$. As the conversions are charge symmetric there is no correlation between the tracks charge and the opposite hemisphere charge. Therefore, for non-prompt electrons

$$\langle Q_{l\rm H} \rangle = 0.0 \ .$$

In this analysis the width is taken from Equation 6.5 using a value of $p_\perp = 0.0$, so that

$$\sigma(Q_{l\rm H}) = 0.416$$

for non-prompt electrons.

6.3 A log likelihood function for the data

The probability density functions derived in the previous sections for both signal and background can now be combined together to create a likelihood function, $\ell(\mathcal{M}_d, \mathcal{M}_s)$, for a single lepton. If $\mathcal{P}_x$ is the probability that the lepton came from process x then

$$\begin{aligned} \ell(\mathcal{M}_d, \mathcal{M}_s) &= \mathcal{P}_b \cdot \ell_b(Q_{l\rm H}, \mathcal{M}_d, \mathcal{M}_s) \\ &+ \mathcal{P}_{bc} \cdot \ell_{bc}(Q_{l\rm H}, \mathcal{M}_d, \mathcal{M}_s) \end{aligned}$$

x	Processes	
b	$b \to e$ or μ $b \to \tau \to e$ or μ $b \to W \to \bar{c} \to e$ or μ	$\mathcal{P}_{bl} + f_W \mathcal{P}_{sc} + \mathcal{P}_{b\tau}$
bc	$b \to c \to e$ or μ	$(1 - f_W)\mathcal{P}_{sc}$
c	$c \to e$ or μ	$\mathcal{P}_c$
np	non-prompt decays	$\mathcal{P}_{\rm np}$
had	misidentified hadrons	$\mathcal{P}_{\rm had}$

Table 6.5: *Definitions of the processes used in equation 6.6. The right hand column shows how the probabilities are derived from those discussed in Section 6.1.2.*

$$+ \quad \mathcal{P}_c \cdot \ell_c(Q_{l\rm H})$$
$$+ \quad \mathcal{P}_{\rm np} \cdot \ell_{\rm np}(Q_{l\rm H}, p, p_\perp, e \text{ or } \mu)$$
$$+ \quad \mathcal{P}_{\rm had} \cdot \ell_{\rm had}(Q_{l\rm H}, p, p_\perp, e \text{ or } \mu) \quad . \tag{6.6}$$

The definition of each process is given in Table 6.5. Also shown in the table is how $\mathcal{P}_x$ is determined from the probabilities discussed in Section 6.1.2, where f_W is the fraction of secondary c decays in the $b \to W \to \bar{c} \to l$ channel. In this analysis f_W is taken to be $(14 \pm 7)\%$ from phase space calculations[47].

A log likelihood function, $\mathcal{L}$, for the sample of leptons created in Section 6.1.5 can now be built from the individual likelihoods,

$$\mathcal{L}(\mathcal{M}_d, \mathcal{M}_s) = \sum_{\text{all leptons}} \ln\left[\ell(\mathcal{M}_d, \mathcal{M}_s)\right] \quad .$$

Contours of this function can then be used to show confidence limits on the $\mathcal{M}_d - \mathcal{M}_s$ plane.

The confidence contours generated from the ALEPH data are shown separately for electrons and muons in Figure 6.6, while the contours for the total sample is shown in Figure 6.7. These results were generated using a κ value of 1.0 as the Monte Carlo was tuned without momentum weighting, i.e. effectively

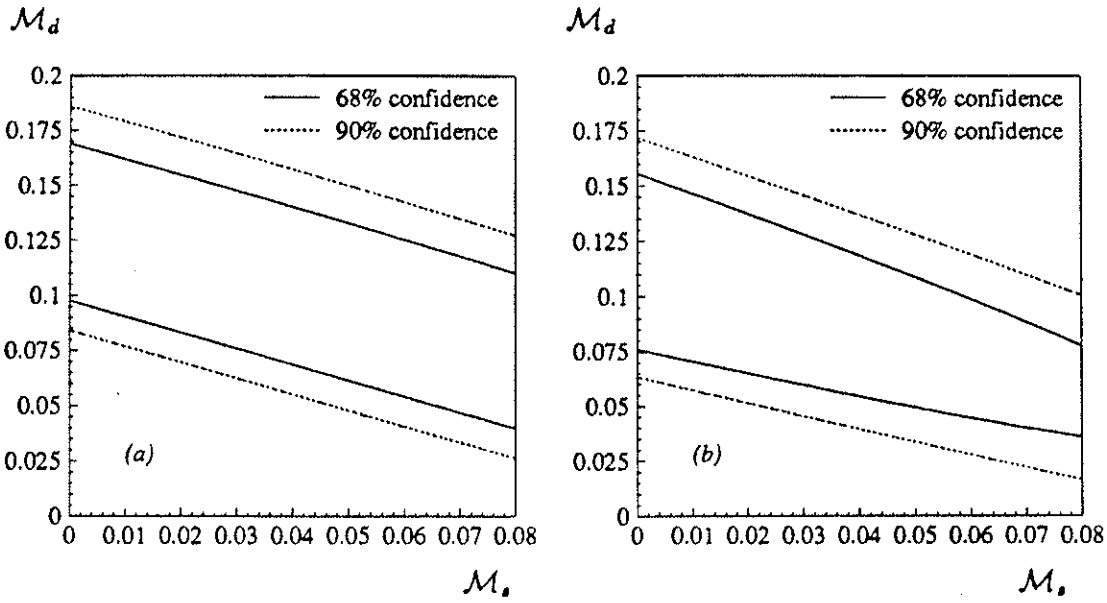

Figure 6.6: *Confidence limits for $\mathcal{M}_d$ and $\mathcal{M}_s$ from (a) electrons (b) muons.*

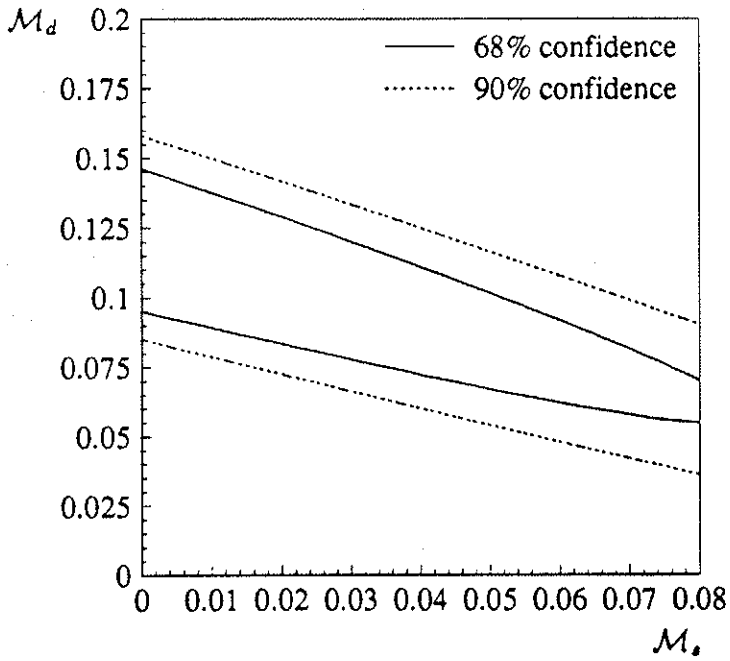

Figure 6.7: *Confidence limits for $\mathcal{M}_d$ and $\mathcal{M}_s$ from combined electrons and muons.*

with $\kappa = 1.0$, and also at this value the hemispheres can be taken as independent (see Section 5.6). The limits on axis are chosen to include maximal mixing within the plane for $f_d < 0.4$ and $f_s < 0.16$.

6.4 Systematic errors

The systematic errors in this method come from various sources. These errors will be treated as if they were Gaussian. A systematic error of $\pm\delta$ in a log likelihood function, caused by varying an input variable by $\pm\Delta$, can be included by rescaling the log likelihood function by a factor $1 + (\delta^2/\sigma^2)$ (see appendix A), where σ is the original error. The value of δ^2/σ^2 can be obtained by calculating $\mathcal{L}'(\mu)$, where $\mathcal{L}'(x)$ is the log likelihood function calculated with the input variable at the limit of its variation and μ is the point of maximum likelihood for the original function. This is the method adopted to calculate the changes to the confidence plot due to the various systematic errors.

For each input variable the value of δ^2/σ^2 is calculated at both the upper and lower bounds. The average value of these two measurements is then used as that variable's contribution to the total value of δ^2/σ^2.

6.4.1 Monte Carlo

The Monte Carlo distributions of $Q_{q\mathrm{H}}$ are a fundamental element of this method. Therefore errors in the Monte Carlo parameter settings and unknown biases in the models will cause an uncertainty in the final result. Moreover there is an error in the parameterisations of $\mathcal{Q}$ simply due to the finite number of Monte Carlo events available.

To measure the effect of the limited Monte Carlo statistics each parameterisation of $\mathcal{Q}$ is moved by an amount equal to the error on its mean. First all the distributions are shifted such that their means are moved away from zero and a new log likelihood is calculated. Then the distributions are moved towards zero and another log likelihood function is calculated. The resulting new functions

are used to determine the statistical contribution to δ^2/σ^2.

To evaluate the uncertainties due to Monte Carlo parameter settings single Gaussians are used to parameterize Q. This is to overcome the problem that the double Gaussian parameters are highly correlated. The fractional changes in the single Gaussian's parameters at generator level (see Section 5.2), caused by a change in one Monte Carlo parameter, are used to change the equivalent Gaussian parameters at reconstructed level. These changed Gaussians are then used to calculate the relevant log likelihood functions and the value of δ^2/σ^2 can then be extracted. If the extracted δ^2/σ^2 due to a parameter change has a greater than 50% chance of being simply a statistical fluctuation, i.e. it is less than 0.455 times the value of δ^2/σ^2 due to statistics, then it is not included in the final value of δ^2/σ^2.

The range of settings used for the Monte Carlo parameters are the same as those in ALEPH's hadron asymmetry paper[48] and the choices are justified in the appendix of that paper. A summary of the production settings, the variations used and their contributions to δ^2/σ^2 are given in Table 6.6.

6.4.2 Lepton Composition

Due to the limited knowledge of semileptonic branching ratios of bottom and charm hadrons there will be some uncertainty in the lepton composition of the sample. To study this the probabilities of each process defined in Table 6.5 are varied. Each process in turn has its probability scaled by the amount given in Table 6.7. Then all the probabilities are renormalised so that they sum to unity. The first three processes' errors are based on the errors in the branching ratios of the dominant channel in that process. The non-prompt and misidentified hadrons fractions are varied according to the limits given in [21]. Included in this study was the uncertainty in f_W. The resulting contributions to δ^2/σ^2 are also shown in Table 6.7.

Parameter	Production Value	Range	δ^2/σ^2
Statistics			0.062
ϵ_b	0.006	0.003—0.010	0.182
ϵ_c	0.020	0.002—0.071	(0.003)
$(\frac{V}{V+PS})_{u,d}$	0.50	0.30—0.75	0.052
$(\frac{V}{V+PS})_s$	0.65	0.50—0.75	(0.006)
$(\frac{V}{V+PS})_{c,b}$	0.75	0.65—0.80	(0.020)
s/u	0.30	0.27—0.40	0.046
b	0.84	0.84—0.93	0.096
σ	0.358	0.340—0.400	0.046
Λ_{QCD}	0.310	0.260—0.400	(0.009)
M_{min}	1.5	1.0—2.0	(0.007)
		Monte Carlo Total	0.484

Table 6.6: *Systematic error contributions from Monte Carlo parameter settings. The numbers given in brackets have a greater than 50% chance of being statistical fluctuations and so are not included in the total. Also shown are the production setting for the parameters and the ranges used for the systematic error study.*

Probability	Percentage Error		δ^2/σ^2
	Electrons	Muons	
$\mathcal{P}_b$	±10		0.031
$\mathcal{P}_{bc}$	±10		0.032
$\mathcal{P}_c$	±15		0.000
$\mathcal{P}_{np}$	±20	±10	0.000
$\mathcal{P}_{had}$	±20	±40	0.000
f_W	±50		0.018
Lepton Composition Total			0.081

Table 6.7: *Systematic error contributions from Lepton composition.*

6.4.3 Baryon fraction

As the mixed and unmixed B_d^0 and B_s^0 mesons' contributions are input into this method separately then the final result is independent of the input values of f_d, f_s, χ_d and χ_s used to generate the Monte Carlo. However the non-B^0 sample is dependent on the ratio R, where

$$R = \frac{f_{\text{baryon}}}{f_u}$$

and f_{baryon} is the fraction of baryons produced. The Monte Carlo settings give a value of $R = 0.23$. No measurement has been made of the quantity at LEP energies, and measurements at lower energies are not particularly useful in evaluating this ratio. Therefore a generous error of ±40% is used. The resulting contribution to δ^2/σ^2 is found to be 0.188.

6.5 Result

The contributions from the systematic error are summarised in Table 6.8. Using the total value of δ^2/σ^2 given in this table the confidence contours, including the

Contribution	δ^2/σ^2
Monte Carlo total	0.484
Lepton composition total	0.081
Baryonic fraction	0.188
Total systematic error	0.753

Table 6.8: *Total systematic error.*

systematic error, can now be plotted. The final contours from the 1989 and 1990 ALEPH data are shown in Figure 6.8.

Using these limits and the definition of χ in Equation 4.7 the 90% confidence limits on χ are

$$0.084 \leq \chi \leq 0.175 \ ,$$

providing $f_s \leq 0.16$

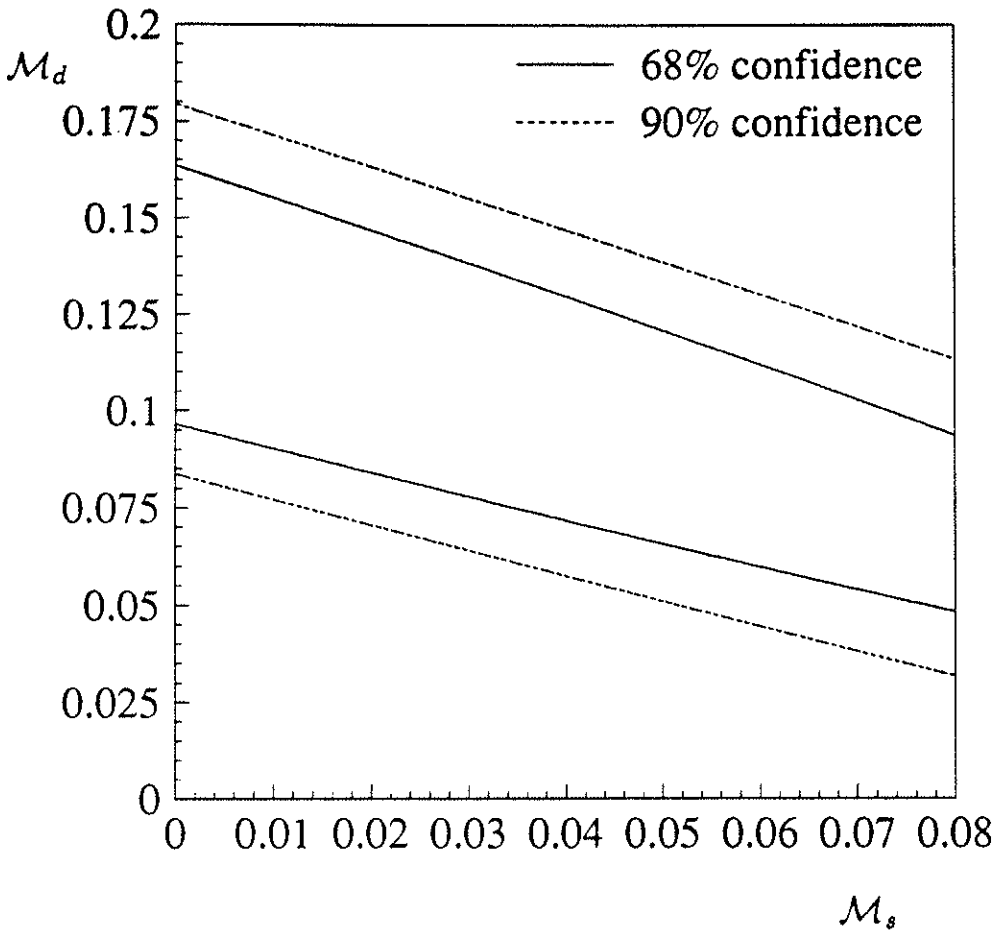

Figure 6.8: *Confidence limit, including systematic errors, for $\mathcal{M}_d$ and $\mathcal{M}_s$ using 1989 and 1990 data from ALEPH.*

Chapter 7

Implications of result

The confidence contours obtained from the present method can be combined with previous measurements of $B^0 - \bar{B}^0$ mixing to give tighter constraints on $\mathcal{M}_d$ and $\mathcal{M}_s$. Throughout this chapter three different measurements of $B^0 - \bar{B}^0$ mixing will be discussed:

1. the hemisphere method described in the thesis;
2. the ALEPH measurement using dileptons[21];
3. The CLEO[18] and ARGUS[9] measurements of r_d.

7.1 ALEPH's dilepton measurement

The confidence limits from ALEPH's dilepton measurement are shown in Figure 7.1. Before the result of the present analysis can be combined with the dilepton result the common statistical and systematic errors have to be taken into account. The dilepton events constitute 8.0% of the events used in the present analysis therefore before combining the results the statistical error of this analysis is scaled by $1/\sqrt{(1-0.08)}$. The common systematic error comes from the uncertainty in the lepton composition of each sample. The contribution to the error from this source is removed from both results before they are combined and then it is added back into the combined result. This method leads to the confidence contours shown in Figure 7.2.

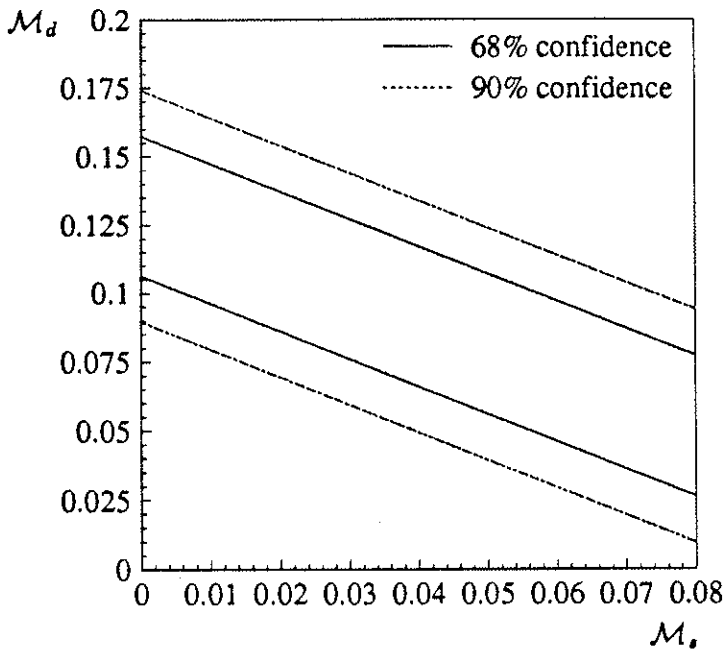

Figure 7.1: *Confidence limits from ALEPH's dilepton measurement of* $B^0 - \bar{B}^0$ *mixing.*

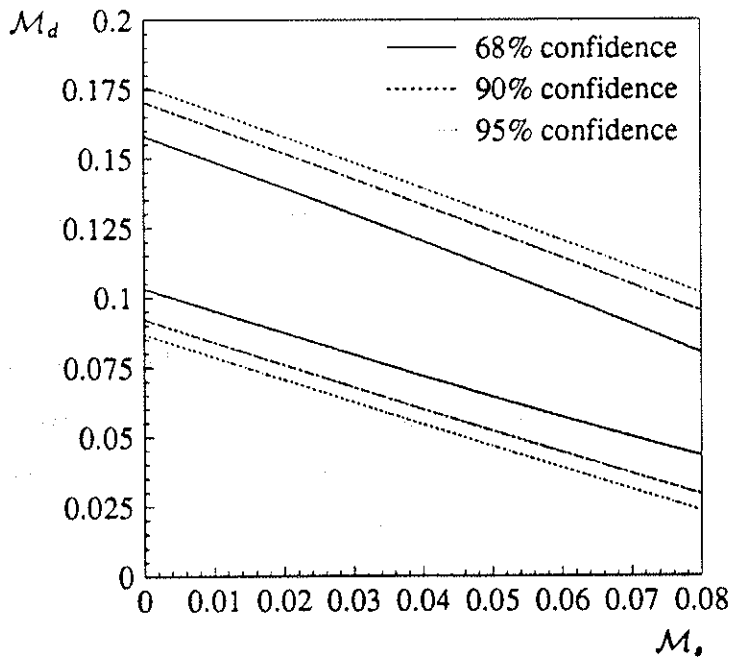

Figure 7.2: *Confidence limits from combining the result of the present analysis with ALEPH's dilepton measurement.*

It can be seen by comparing Figures 6.8 and 7.1 that the underlying slopes on the $\mathcal{M}_d - \mathcal{M}_s$ plane are different. This is caused by the fact that $\mathcal{A}_{sep}$ for B_d^0's and B_s^0's are different so that $\mathcal{M}_d$ and $\mathcal{M}_s$ enter the hemisphere charge contribution to the present method with different coefficients, whereas the lepton contributions in both methods have the same coefficients for $\mathcal{M}_d$ and $\mathcal{M}_s$. This feature may become significant in reducing the errors on $\mathcal{M}_d$ and $\mathcal{M}_s$ when substantially more data has been collected by ALEPH.

7.2 r_d measurement from CLEO and ARGUS

The average result of r_d measured by CLEO and ARGUS is

$$r_d = 0.20 \pm 0.06 \ .$$

This corresponds to a value of

$$\chi_d = 0.167 \pm 0.042 \ . \tag{7.1}$$

To interpret this in terms of $\mathcal{M}_d$ the fraction f_d must be known. At present this is not well known but the standard choice at LEP energies is[21][22]

$$f_d = 0.375 \pm 0.050 \ . \tag{7.2}$$

Combining this with Equation 7.1 gives

$$\mathcal{M}_d = 0.063 \pm 0.018 \ .$$

The confidence contours for this measurement are shown in Figure 7.3.

Taking the errors on this measurement to be independent of both methods 1 and 2, the CLEO/ARGUS result can be combined with the result of method 1 to give the confidence contours shown in Figure 7.4. Combining the CLEO/ARGUS result with the results of methods 1 and 2 gives the confidence contours shown in Figure 7.5. From this figure it can be seen that at the 90% confidence limit

$$\mathcal{M}_s > 0.011 \ . \tag{7.3}$$

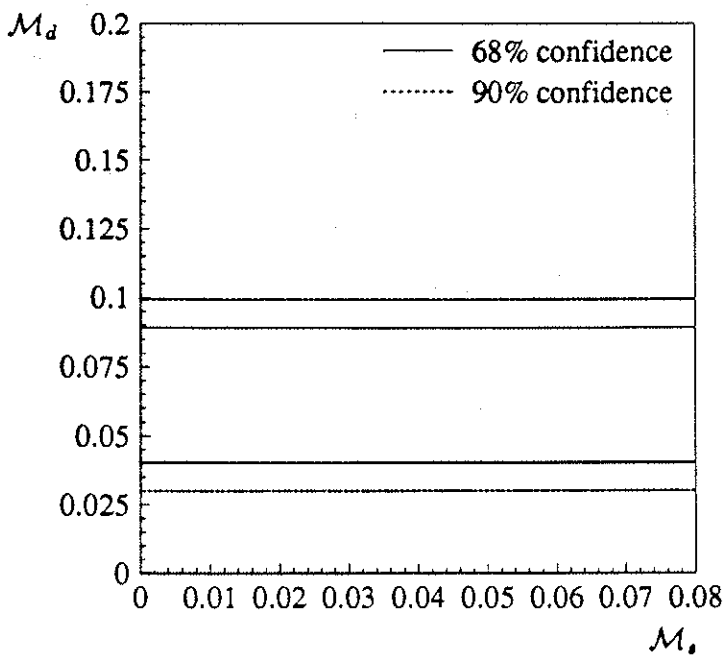

Figure 7.3: *Confidence limits on $\mathcal{M}_d$ using the average r_d measurement from CLEO and ARGUS.*

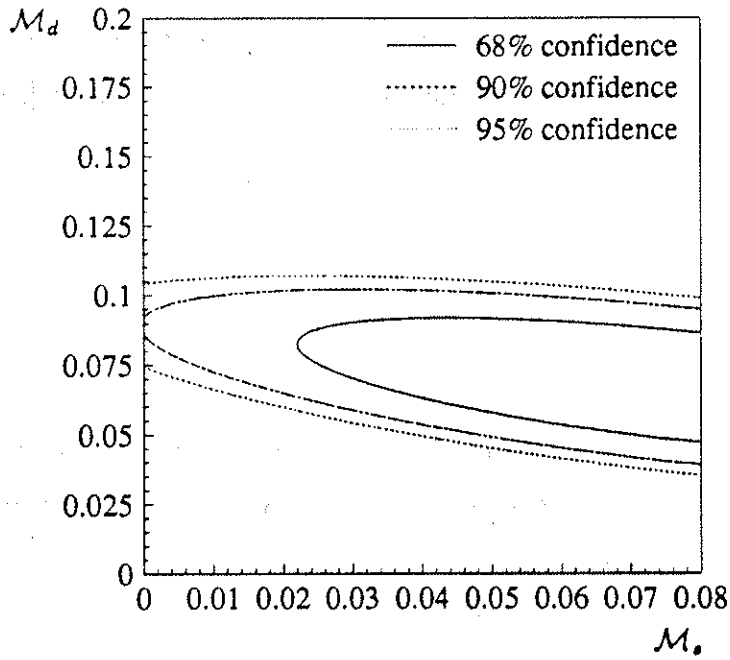

Figure 7.4: *Confidence limits from combining the result of the present analysis with the CLEO/ARGUS measurement of r_d.*

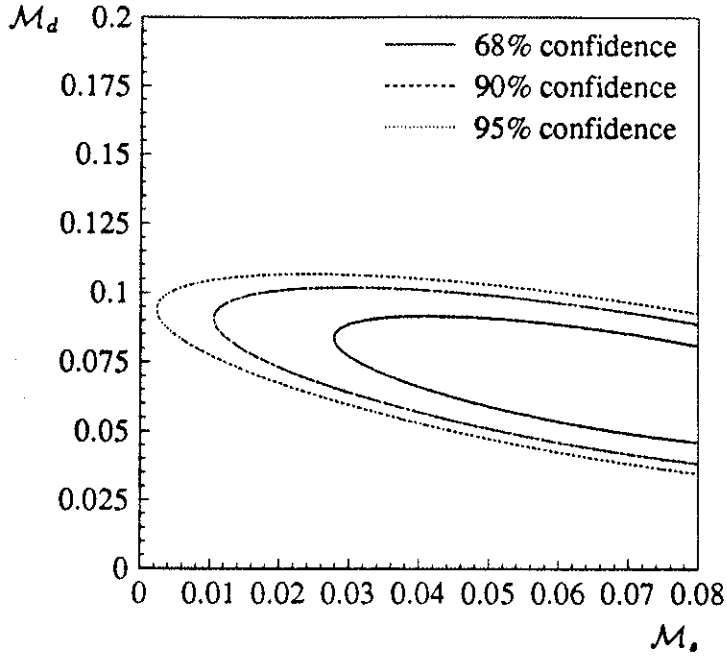

Figure 7.5: *Confidence limits from combining the result all three methods discussed in this chapter.*

Using the combined result gives the following measurements for $\mathcal{M}_d$ and $\mathcal{M}_s$,

$$\mathcal{M}_d = 0.068 \pm 0.016 \tag{7.4}$$

$$\mathcal{M}_s = 0.067 \pm 0.026 \ . \tag{7.5}$$

To interpret these contours in terms of χ_d and χ_s the fractions of B_d^0 and B_s^0 have to be known. Equation 7.2 gives the standard value for f_d, and the standard value for f_s is

$$f_s = 0.150 \pm 0.050 \ . \tag{7.6}$$

The combined result of methods 1, 2 and 3 is shown in Figure 7.6 including the χ_d and χ_s values assuming these fractions. The shaded region of this figure shows the region allowed by the Standard Model (see Equation 4.4).

Combining Equations 7.2 and 7.3 gives

$$\chi_s > 0.07 \ .$$

at the 90% confidence level. Similarly Equations 7.2 and 7.4 and Equations 7.5

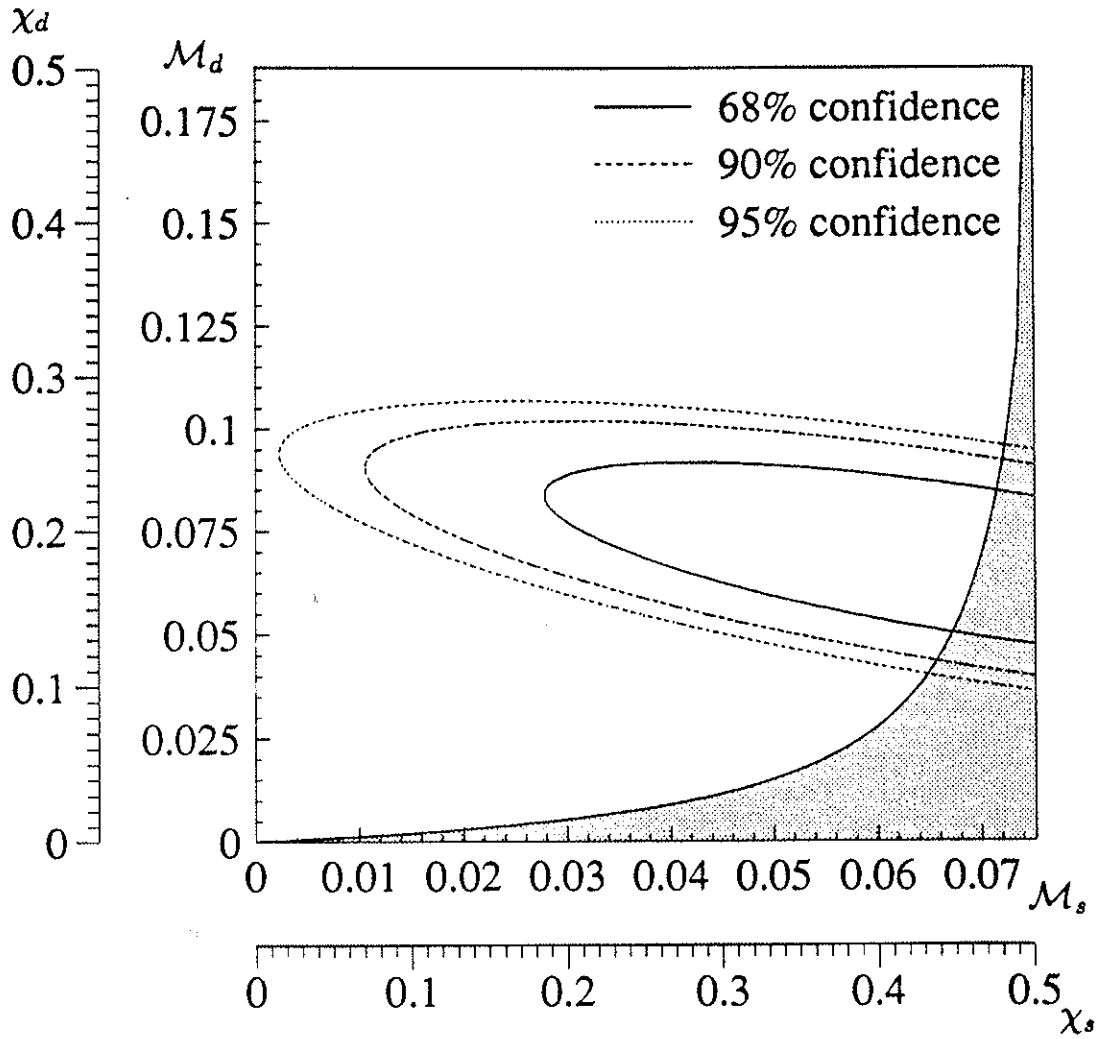

Figure 7.6: *Confidence limits for χ_d and χ_s assuming $f_d = 0.375$ and $f_s = 0.150$. The shaded region shows the area allowed by the Standard Model.*

and 7.6 give

$$\chi_d = 0.18 \pm 0.05$$
$$\chi_s = 0.45 \pm 0.24 \ .$$

It should be remembered that only values of $0.0 \leq \chi_q \leq 0.5$ are physically meaningful.

References

[1] Particle Data Group, Phys. Lett. **B239** (1990) 1–516.

[2] W. Blum, editor. *The Aleph Handbook.* ALEPH-Note 89-03 (unpublished), 1989.

[3] ALEPH collab., D. Decamp *et al.*, Nucl. Instr. and Meth. **A294** (1990) 121–178.

[4] W. B. Atwood *et al.*, CERN PPE/91–24(Submitted to Nucl. Instr. and Meth. A) .

[5] ALEPH collab., D. Decamp *et al.*, CERN PPE/91–129(Submitted to Z. Phys. C) .

[6] B. Cameron, K. Smith, and R. St.Denis. ALEPH run quality information for the spring 1990 data taking. ALEPH-Note 90–80 (unpublished).

[7] G. J. Barber *et al.*, Nucl. Instr. and Meth. **A279** (1989) 212–216.

[8] F. Dydak, CERN PPE/91–14(Rapporteur's talk given at 25th International Conference on High Energy Physics in Singapore) .

[9] ARGUS collab., H. Albrecht *et al.*, Phys. Lett. **B192** (1987) 245–252.

[10] G. Altarelli and P. J. Franzini, Z. Phys. **C37** (1988) 271–280.

[11] F. Abe *et al.*, Phys. Rev. Lett. **64** (1989) 143–146.

[12] A. Blondel, CERN PPE/90-10(Submitted to Phys. Lett. B) .

[13] N. Cabibbo, Phys. Rev. Lett. **10** (1963) 531–533.

[14] M. Kobayashi and T. Maskawa, Prog. Theor. Phys. **49** (1973) 652–657.

[15] P. Franzini, Phys. Reps. **173** (1989) 1–62.

[16] S. Narison, Phys. Lett. **B198** (1987) 104–112.

[17] C. Bernard *et al.*, Phys. Rev. **D38** (1988) 3540–3549.

[18] CLEO collab., M. Artuso *et al.*, Phys. Rev. Lett. **62** (1989) 2233–2236.

[19] MAC collab., H. R. Band *et al.*, Phys. Lett. **B200** (1988) 221–225.

[20] UA1 collab., C. Albajar *et al.*, Phys. Lett. **B186** (1987) 247–254.

[21] ALEPH collab., D. Decamp *et al.*, Phys. Lett. **B258** (1991) 236–246.

[22] L3 collab., B. Adeva *et al.*, Phys. Lett. **B252** (1990) 703–712.

[23] J. H. Christenson *et al.*, Phys. Rev. Lett. **13** (1964) 138.

[24] C.S.Kim, J.L. Rosner, and C.-P.Yuan, Phys. Rev. **D42** (1990) 96–111.

[25] T. Sjöstrand, Comp. Phy. Comm. **39** (1986) 347–407.

[26] T. Sjöstrand. The Lund Monte Carlo for jet fragmentation and e^+e^- physics – JETSET version 6.3 – an update. Lund preprint; LU TP 86-22.

[27] B. Bloch *et al.* KINGAL User's Guide. ALEPH-Note 91–82 (unpublished).

[28] F. Ranjard *et al.* GALEPH User's Guide. ALEPH-Note 90–119 (unpublished).

[29] R. Brun *et al.* GEANT 3 User's Guide. CERN DD/EE/84-1.

[30] G. Altarelli and G. Parisi, Nucl. Phys. **B126** (1977) 298.

[31] B. Anderson, G. Gustafson, and C. Peterson, Z. Phys. **C1** (1979) 105–116.

[32] B. Anderson, G. Gustafson, and C. Söderberg, Z. Phys. **C20** (1983) 317–329.

[33] C. Peterson *et al.*, Phys. Rev. **D27** (1983) 105–111.

[34] ALEPH collab., D. Decamp *et al.*, Phys. Lett. **B244** (1990) 551–565.

[35] R. D. Field and R. Feynman, Nucl. Phys. **B136** (1978) 1–76.

[36] PLUTO collab., Ch. Berger *et al.*, Nucl. Phys. **B214** (1983) 189–200.

[37] MAC collab., W. W. Ash *et al.*, Phys. Rev. Lett. **58** (1987) 1080–1083.

[38] JADE collab., T. Greenshaw *et al.*, Z. Phys. **C42** (1989) 1–5.

[39] AMY collab., D. Stuart *et al.*, Phys. Rev. Lett. **64** (1990) 983–986.

[40] I. Adachi. *Measurements of total Cross Section and Charge Asymmetry of Hadronic Events in e^+e^- Annihilations at TRISTAN.* PhD thesis, Nagoya University, 1990.

[41] A. Blondel and E. Blucher. Hadronic–event selection with charged tracks. ALEPH-Note 90–171 (unpublished).

[42] TASSO collab., M.Althoff *et al.*, Phys. Lett. **B149** (1984) 524–532.

[43] TASSO collab., W. Braunschweig *et al.*, Z. Phys. **C42** (1989) 189.

[44] JADE collab., W.Bartel *et al.*, Z. Phys. **C33** (1986) 23–31.

[45] ALEPH collab., D. Decamp *et al.*, Phys. Lett. **B263** (1991) 325–336.

[46] Anjos *et al.*, Phys. Rev. Lett. **60** (1988) 1239–1242.

[47] C. Quigg and J. L. Rosner, Phys. Rev. **D19** (1979) 1532–1542.

[48] ALEPH collab., D. Decamp *et al.*, Phys. Lett. **B259** (1991) 377–388.